Cohesin supercoils DNA during loop extrusion

Davidson, Iain F.; Barth, Roman; Nagasaka, Kota; Tang, Wen; Wutz, Gordana; Horn, Sabrina; Janissen, Richard; Dekker, Cees; Peters, Jan Michael

DOI
10.1016/j.celrep.2025.115856

Publication date
2025

Document Version
Final published version

Published in
Cell Reports

Citation (APA)
Davidson, I. F., Barth, R., Nagasaka, K., Tang, W., Wutz, G., Horn, S., Janissen, R., Dekker, C., & Peters, J. M. (2025). Cohesin supercoils DNA during loop extrusion. *Cell Reports*, *44*(6), Article 115856. https://doi.org/10.1016/j.celrep.2025.115856

Cell Reports

Cohesin supercoils DNA during loop extrusion

Graphical abstract

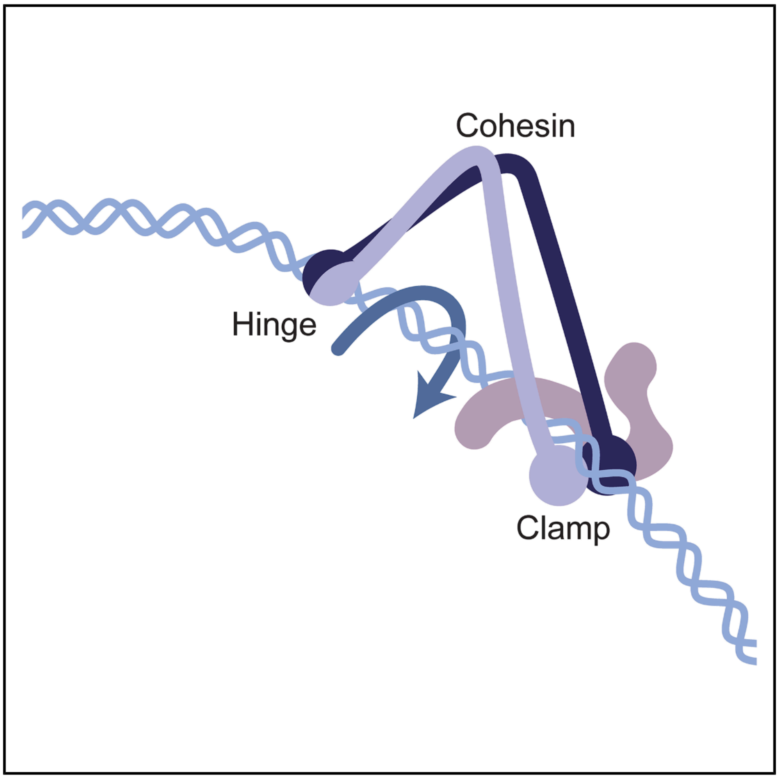

Authors

Iain F. Davidson, Roman Barth,
Kota Nagasaka, ..., Benedikt W. Bauer,
Cees Dekker, Jan-Michael Peters

Correspondence

peters@imp.ac.at

In brief

Davidson et al. show that cohesin negatively supercoils DNA. *In vitro*, this process depends on the same DNA-binding sites and co-factors as cohesin's loop-extrusion activity, and a cohesin mutant defective in negative supercoiling forms shorter loops in cells. These results indicate that cohesin supercoils DNA during loop extrusion.

Highlights

- Cohesin twists DNA while constraining it between the hinge and the clamp
- The torque required for twisting depends on the DNA-binding affinity of the clamp
- Topoisomerase I is required for formation of long cohesin loops in cells

Davidson et al., 2025, Cell Reports *44*, 115856
June 24, 2025
https://doi.org/10.1016/j.celrep.2025.115856

CellPress

Cell Reports

CellPress
OPEN ACCESS

Article

Cohesin supercoils DNA during loop extrusion

Iain F. Davidson,[1] Roman Barth,[2,4,5] Kota Nagasaka,[1] Wen Tang,[1] Gordana Wutz,[1] Sabrina Horn,[1,3] Richard Janissen,[2,6]
Roman R. Stocsits,[1] Emilia Chlosta,[1] Benedikt W. Bauer,[1,7] Cees Dekker,[2] and Jan-Michael Peters[1,8,*]
[1]Research Institute of Molecular Pathology, Vienna BioCenter, Vienna, Austria
[2]Department of Bionanoscience, Kavli Institute of Nanoscience Delft, Delft University of Technology, Delft, the Netherlands
[3]Vienna BioCenter PhD Program, Doctoral School of the University of Vienna and Medical University of Vienna, Vienna, Austria
[4]Present address: Department of Biochemistry, University of Washington, Seattle, WA, USA
[5]Present address: Institute for Protein Design, University of Washington, Seattle, WA, USA
[6]Present address: Institute of Bioengineering, Deggendorf Institute of Technology, Oberschneiding, Germany
[7]Present address: BioNTech R&D Austria, Vienna
[8]Lead contact
*Correspondence: peters@imp.ac.at
https://doi.org/10.1016/j.celrep.2025.115856

SUMMARY

Cohesin extrudes genomic DNA into loops that promote chromatin assembly, gene regulation, and gene recombination. Loop extrusion depends on large-scale conformational changes in cohesin, but how these translocate DNA is poorly understood. Here, we provide evidence that cohesin negatively supercoils DNA during loop extrusion. Supercoiling requires the engagement of cohesin's ATPase heads, DNA clamping by these heads, and a DNA-binding site on cohesin's hinge, indicating that cohesin twists DNA when constraining it between the hinge and the clamp. A cohesin mutant defective in negative supercoiling forms shorter loops in cells, and a similar, although weaker, phenotype is observed after the depletion of topoisomerase I. These results suggest that supercoiling is an integral part of the loop-extrusion mechanism and that relaxation of supercoiled DNA is required for cohesin-mediated loop extrusion and genome architecture.

INTRODUCTION

In eukaryotic interphase cells, the "structural maintenance of chromosomes" (SMC) complex cohesin folds genomic DNA into loops and topologically associating domains (TADs[1–4]), which can regulate transcription,[5] recombination,[6,7] local sister chromatid separation,[8] and replication.[9] Cohesin extrudes DNA into loops[10,11] through conformational changes that are controlled by ATP-binding-hydrolysis cycles[12] (reviewed in Dekker et al.[13]). These are catalyzed by cohesin's SMC1 and SMC3 subunits, which contain 50-nm-long coiled coils, dimerization hinge domains, and globular ATPase heads (Figure S1A), which are related to those of ABC transporters.[14] Upon ATP binding, cohesin's heads engage, and a subunit called Nipped-B-like protein (NIPBL) clamps DNA on top of the engaged ATPase heads[12,15–17] (Figures S1A and S1B). These movements generate ∼15 pN force[18] and loop-extrusion steps of ∼40 nm (100–200 bp[19]), suggesting that DNA is reeled into the forming loop during head engagement.

In contrast, little is known about conformational changes of DNA during loop extrusion. Topoisomerase II binds and cleaves DNA at the base of cohesin loops,[20–23] suggesting that DNA is supercoiled at these sites. It has been proposed that supercoils generated elsewhere in the genome by transcription become trapped at the base of cohesin loops,[22] but it has been pointed out that cohesin itself could also generate such supercoils during loop extrusion.[20] The related mitotic SMC complex condensin can supercoil DNA *in vitro*,[24–26] also co-localizes and interacts with topoisomerases,[27–33] and has recently been proposed to supercoil DNA during loop extrusion.[24,26] However, cohesin was found not to supercoil DNA,[34] even though cohesin and condensin are thought to use similar loop-extrusion mechanisms.[13] It has therefore remained unclear whether DNA is generally supercoiled during loop extrusion or whether topoisomerases accumulate at the base of SMC loops for other reasons. If DNA is indeed supercoiled during loop extrusion, it is unknown during which step of the loop-extrusion cycle this occurs, and it has not been tested whether this supercoiling activity is required for cohesin's DNA loop-extrusion function in cells.

RESULTS

Cohesin and NIPBL supercoil DNA

We therefore tested whether cohesin can supercoil DNA in the presence of NIPBL, which is essential for loop extrusion but was not included in earlier experiments.[34] For this purpose, we used an assay that measures changes in the linking number (L_k) of plasmids.[25] L_k describes the number of times one strand passes over the other and is the sum of helical turns (or twist, Tw) and superhelical turns (or writhe, Wr; a DNA segment is called a plectoneme if multiple writhes accumulate within it). For topologically constrained DNA molecules, L_k is invariant, i.e., any increase in Tw is compensated for by a decrease in Wr and vice versa. However, L_k can be altered by topoisomerases, which introduce DNA breaks, allow the DNA strands to rotate around each other, and reseal the breaks. If cohesin

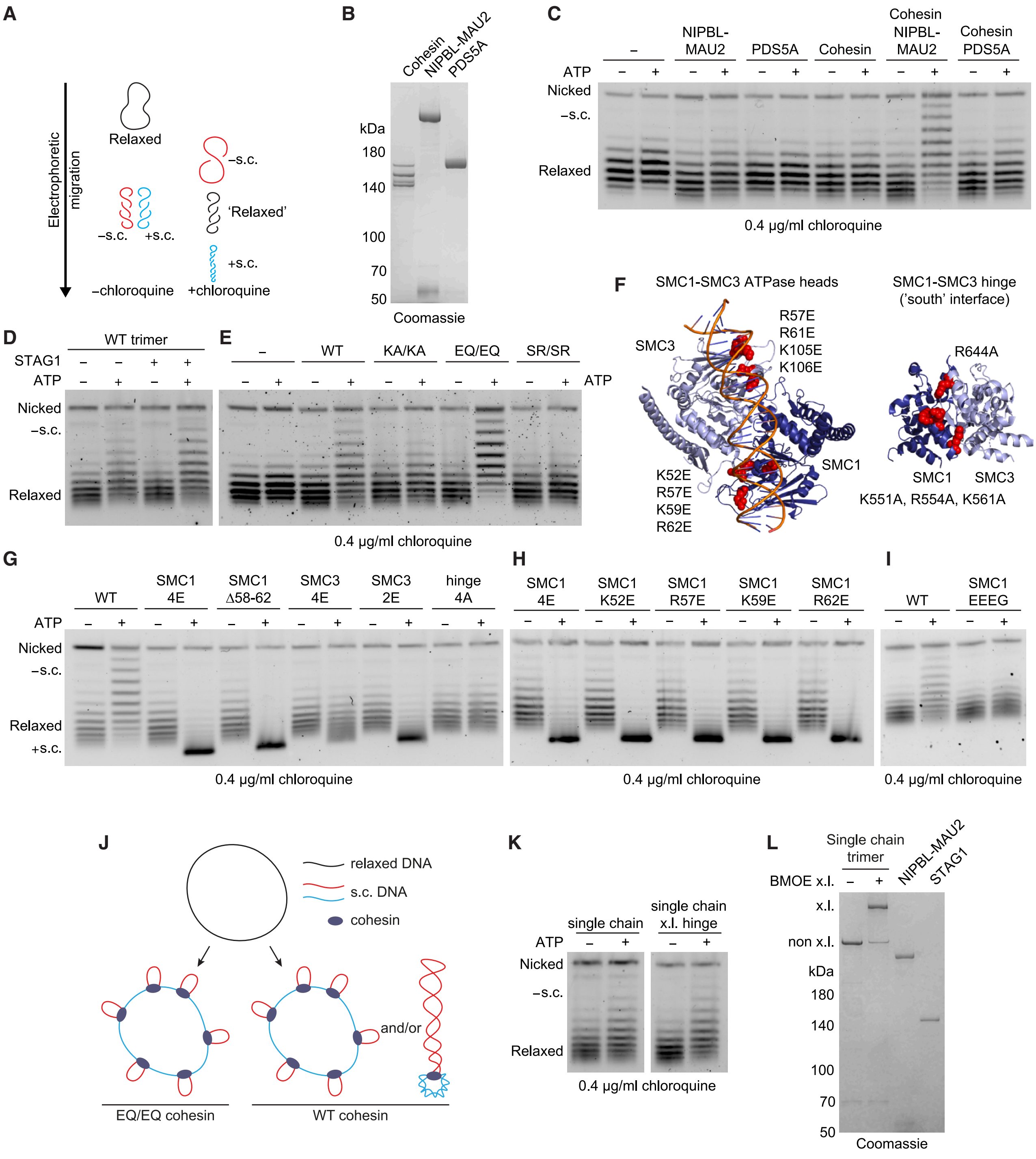

Figure 1. Cohesin supercoils DNA during clamping

(A) Chloroquine agarose gel electrophoresis allows discrimination between negatively and positively supercoiled plasmid DNA.

(B) Coomassie staining of recombinant human cohesin, NIPBL-MAU2, and PDS5A after SDS-PAGE.

(C) Plasmid supercoiling assay. Negatively supercoiled plasmid DNA was relaxed by incubating with human topoisomerase I. Reactions were then supplemented as indicated with ATP, wild-type cohesin at a 15:1 cohesin/plasmid ratio, NIPBL-MAU2 (30:1 NIPBL-MAU2/plasmid ratio), or PDS5A (30:1 PDS5A/plasmid ratio). Reactions were terminated, and purified DNA was separated by chloroquine agarose gel electrophoresis.

(D) As in (C), except trimeric cohesin was added at a 15:1 cohesin/plasmid ratio along with NIPBL-MAU2 (30:1 NIPBL-MAU2/plasmid ratio). Incubations were supplemented as indicated with ATP and STAG1 (30:1 STAG1/plasmid ratio).

(legend continued on next page)

supercoils DNA and thus generates topological stress (changes in Tw or Wr) that are relaxed by a topoisomerase, the plasmid's L_k will change. This change in linking number, ΔL_k, affects the shape and hydrodynamic radius of plasmids and can therefore be detected by a change in their electrophoretic mobility (Figure 1A).

Supercoiling can occur in two orientations. In relaxed DNA, the two strands twist around its helical axis in a right-handed manner once every ~10.5 bp.[35] DNA molecules that are more or less twisted than this are "positively" or "negatively" supercoiled, respectively. The handedness of supercoiling can be detected by electrophoresis in the presence of the DNA intercalator chloroquine. Chloroquine induces positive supercoiling, and thus causes positively supercoiled plasmids to migrate faster than relaxed DNA and negatively supercoiled DNA to migrate more slowly[36] (Figure 1A).

To analyze cohesin's supercoiling activity, we used human topoisomerase I (Figures S1C and S1D), which relaxes negative and positive supercoils. In this assay, human tetrameric cohesin (containing SMC1, SMC3, the kleisin subunit SCC1, and STAG1; Figures 1B and S1E) did not alter the electrophoretic mobility of relaxed plasmids (Figure 1C), as reported previously.[34] However, when NIPBL-MAU2 (Figure 1B) was added, more slowly migrating DNA bands appeared in an ATP- and topoisomerase I-dependent manner (Figures 1C, S1F, and S1G), indicating that cohesin generates negatively supercoiled plasmids in the presence of NIPBL-MAU2. This was not the case when NIPBL-MAU2 was replaced by PDS5A (Figures 1B and 1C). Unless otherwise stated, all subsequent supercoiling experiments were therefore performed in the presence of NIPBL-MAU2. Since cohesin's loop-extrusion activity also depends on ATP and NIPBL-MAU2[10,11] and is not supported by PDS5A,[10] these results suggest that cohesin supercoils DNA during loop extrusion. Supporting this possibility, we found that STAG1, which is required for loop extrusion,[10] also stimulates cohesin's supercoiling activity (Figure 1D).

Cohesin supercoils DNA during clamping

To understand at which step of its ATP binding-hydrolysis cycle cohesin supercoils DNA, we analyzed the effect of mutations in the Walker A motifs (K38A/K38A, hereafter KA/KA), the signature motifs (S1129R/S1116R; SR/SR), and the Walker B motifs (E1157Q/E1144Q; EQ/EQ) of SMC1 and SMC3. These mutations block ATP binding, head dimerization, and ATP hydrolysis, respectively.[14,37] We found that supercoiling was inhibited by KA/KA and SR/SR but not by the EQ/EQ mutations (Figure 1E), indicating that supercoiling depends on ATP-dependent head engagement but not on subsequent ATP hydrolysis. Since cryogenic electron microscopy (cryo-EM[15–17]) and single-molecule Förster resonance energy transfer experiments (smFRET[12]) have suggested that EQ/EQ mutations stabilize the head-engaged state of cohesin in which DNA is clamped onto the ATPase heads by NIPBL, these results indicate that cohesin induces supercoiling during DNA clamping.

To test this hypothesis, we analyzed cohesin in which the DNA-binding sites on the ATPase heads of SMC1 ($SMC1^{4E}$) or SMC3 ($SMC3^{4E}$) were mutated[12] (Figure 1F) and which are therefore predicted to be defective in DNA clamping. Indeed, no slowly migrating DNA bands were detected in the presence of these complexes, suggesting that cohesin mutants that are defective in DNA clamping are also defective in generating negatively supercoiled DNA (Figure 1G).

However, these experiments revealed an unexpected phenomenon. Supercoiling reactions containing cohesin-$SMC1^{4E}$ were not defective in generating slowly migrating DNA but instead greatly increased the electrophoretic mobility of plasmids in an ATP- and topoisomerase I-dependent manner, indicating that they became positively supercoiled (Figures 1G, S1F, and S1G). A 5-amino-acid deletion in SMC1 that includes two of the residues mutated in $SMC1^{4E}$ ($SMC1^{\Delta 58-62}$) had a similar effect (Figure 1G). Remarkably, charge reversal of K52, R57, K59, and R62 alone also caused positive supercoiling (Figure 1H). These residues are located in a loop that contains the "arginine finger" R57, which is required for the DNA-dependent ATPase activity of *B. subtilis* SMC (R57 in human SMC1 corresponds to R59 in *B. subtilis* SMC[38]).

Fast-migrating DNA was also observed after incubation with cohesin-$SMC3^{2E}$ and to a lesser extent with cohesin-$SMC3^{4E}$ (Figure 1G). The overall reduction of supercoiling in the presence of cohesin-$SMC3^{4E}$ is presumably due to the fact that this mutant binds DNA even less well than cohesin-$SMC1^{4E}$ and cohesin-$SMC3^{2E}$, as is indicated by the degrees by which the DNA-dependent ATPase activities of these mutants are reduced.[12] To test this, we combined the $SMC1^{4E}$ and $SMC3^{4E}$ mutations to

---

(E) As in (C), except wild-type, K38A/K38A, E1157Q/E1144Q, or S1129R/S1116R cohesin were added at a 20:1 cohesin/plasmid ratio. NIPBL-MAU2 was added to all reactions (40:1 NIPBL-MAU2/plasmid ratio).

(F) Structures of the SMC1–SMC3 ATPase heads (left; PDB: 6WG3) and hinge (right; PDB: 2WD5). DNA-binding-site mutations are indicated as spheres.[12]

(G) As in (C), except wild-type, $SMC1^{4E}$ (K52E, R57E, K59E, R62E), $SMC1^{\Delta 58-62}$, $SMC3^{4E}$ (R57E, R61E, K105E, K106E), $SMC3^{2E}$ (R57E, R61E), or hinge 4A (SMC1 K551A, R554A, K561A; SMC3 R644A) cohesin was added at a 15:1 cohesin/plasmid ratio. NIPBL-MAU2 was added to all reactions (30:1 NIPBL-MAU2/plasmid ratio).

(H) As in (C), except the indicated forms of cohesin were added at a 15:1 cohesin/plasmid ratio. NIPBL-MAU2 was added to all reactions (30:1 NIPBL-MAU2/plasmid ratio).

(I) As in (C), except the indicated forms of cohesin were added at a 10:1 cohesin/plasmid ratio. NIPBL-MAU2 was added to all reactions (20:1 NIPBL-MAU2/plasmid ratio).

(J) The plasmid supercoiling assay cannot distinguish between a single cohesin introducing multiple supercoils into a plasmid and multiple cohesin complexes each introducing some twist (the latter is predicted to be the case for $cohesin^{EQ/EQ}$).

(K) As in (C), except single-chain cohesin treated with BMOE (x.l. hinge) or treated with pre-quenched BMOE (not x.l.) were added at a 10:1 cohesin/plasmid ratio. NIPBL-MAU2 and STAG1 were added to all reactions at 20:1 protein/plasmid ratios.

(L) Coomassie staining of single-chain cohesin, NIPBL-MAU2, and STAG1 used in (K) after SDS-PAGE.

See also Figure S1.

generate cohesin-SMC1^{4E}-SMC3^{4E}, which is predicted to be further reduced in DNA clamping. No supercoiling could be detected in the presence of cohesin-SMC1^{4E}-SMC3^{4E}, supporting the interpretation that cohesin's supercoiling activity depends on DNA clamping (Figure S1H). Cohesin's ability to generate either negatively or positively supercoiled plasmids was also abolished by mutation of a DNA-binding site on cohesin's hinge (hinge^{4A})[12] (Figure 1G), indicating that this DNA-binding site is also required for supercoiling.

These results suggest that weakening the DNA-binding sites of the clamp results in a switch from negative to positive supercoiling, whereas reducing DNA binding more strongly either in the clamp or at the hinge prevents supercoiling. These results are also consistent with the hypothesis that cohesin supercoils DNA during loop extrusion, since all mutants defective in negative supercoiling are also reduced in their ability to extrude DNA.[12]

To further test whether cohesin supercoils DNA during loop extrusion, we analyzed another cohesin mutant that is defective in this process. In this variant, mutation of four negatively charged residues within the coiled coil of SMC1 (R693E, R711E, R790E, and R816G, referred to here as SMC1^{EEEG}) prevents cohesin from aligning its coiled coils and inhibits its ability to extrude DNA loops.[12] SMC1^{EEEG} was also strongly defective in the plasmid supercoiling assay (Figure 1I), further supporting the hypothesis that cohesin supercoils DNA during loop extrusion.

It is important to note that the plasmid supercoiling assay cannot distinguish between a single cohesin molecule being able to introduce multiple supercoils into a plasmid or multiple cohesin complexes binding to a plasmid and each introducing some twist. In the case of cohesin$^{EQ/EQ}$, the latter must be the case, since this mutant cannot hydrolyze ATP and extrude DNA into loops.[10] However, single wild-type cohesin complexes might be able to introduce multiple supercoils into plasmids during successive ATP binding-hydrolysis and loop-extrusion cycles (Figure 1J). This interpretation is supported by magnetic tweezers experiments, which indicate that wild-type cohesin can twist DNA during successive loop-extrusion steps, whereas cohesin$^{EQ/EQ}$ can only induce a single step of DNA twisting.[39]

DNA clamping is thought to be an intermediate step of the loop-extrusion cycle, since mutation of the DNA-binding sites that mediate DNA clamping reduces loop extrusion[12] and since cohesin's ATP-binding-hydrolysis cycles promote both loop extrusion[10,11] and assembly-disassembly cycles of the DNA clamp.[12,15–17] However, cohesin$^{EQ/EQ}$, which stabilizes the clamped state, has also been proposed to entrap DNA topologically inside a ring structure that is formed by its subunits SMC1, SMC3, and SCC1.[40] This type of DNA interaction is required for cohesin's ability to connect replicated DNA molecules, i.e., to mediate sister chromatid cohesion.[41] Our finding that DNA clamping is required for supercoiling therefore raised the possibility that cohesin supercoils DNA when entrapping it topologically.

To test this possibility, we used a version of cohesin that cannot open the three interfaces between its ring-forming subunits and thus cannot entrap DNA topologically. In this "single-chain" cohesin, the SMC-kleisin interfaces are covalently connected via peptide linkers and the SMC1-SMC3 hinge can be chemically crosslinked via engineered cysteine residues by BMOE treatment. This form of cohesin is an active ATPase and loop extruder in the absence and presence of hinge crosslinking.[10] We found that single-chain cohesin induced the formation of negatively supercoiled plasmids in an ATP-dependent manner. Importantly supercoiling was not inhibited by BMOE treatment, which induced hinge crosslinking with 82% ± 0.5% efficiency (Figures 1K and 1L).

These results suggest that topological entrapment of DNA is not required for plasmid supercoiling. Since loop extrusion can also occur without DNA entrapment,[10] these observations support the hypothesis that supercoiling occurs during loop extrusion. However, these results do not exclude the possibility that cohesin could, in addition, supercoil DNA during DNA entrapment or during other modes of cohesin-DNA interactions, such as active translocation of cohesin along DNA.[10]

Visualization of cohesin-mediated DNA supercoiling using HS-AFM

To confirm that plasmids incubated with cohesin and topoisomerase I become supercoiled, we re-isolated these plasmids, visualized them by high-speed atomic force microscopy (HS-AFM), and counted the number of DNA crossings per plasmid (Figures 2A–2E and S2; Videos S1 and S2). Plasmids that had previously been incubated with cohesin displayed a higher number of DNA crossings, and cohesin$^{EQ/EQ}$ and cohesin-SMC1^{4E} induced more DNA crossings than wild-type cohesin (Figures 2C–2E and S2). These results support the interpretation that wild-type cohesin, cohesin$^{EQ/EQ}$, and cohesin-SMC1^{4E} all induce supercoiling (where we note that negatively and positively supercoiled plasmids cannot be distinguished in these HS-AFM data).

Analysis of plasmid supercoiling handedness

We next tested whether the plasmids generated in the presence of cohesin-SMC1^{4E} were indeed positively supercoiled, as we assumed in our interpretations above. Notably, highly negatively supercoiled plasmids can also have an increased electrophoretic mobility if the number of negative supercoils exceeds the number of positive supercoils induced by chloroquine (Figure S1D). We therefore analyzed plasmids supercoiled in the presence of topoisomerase I and wild-type cohesin, cohesin$^{EQ/EQ}$, or cohesin-SMC1^{4E} by two-dimensional gel electrophoresis in the presence of chloroquine. These experiments confirmed that predominantly negatively supercoiled plasmids are generated in the presence of wild-type cohesin and cohesin$^{EQ/EQ}$, whereas positively supercoiled plasmids are generated in the presence of cohesin-SMC1^{4E} (Figure 2F).

This conclusion was also supported by experiments in which we re-isolated plasmids supercoiled in the presence of topoisomerase I and cohesin-SMC1^{4E} or cohesin$^{EQ/EQ}$ and subsequently treated them with topoisomerases, which preferentially relax positive supercoils topoisomerase IV (Topo IV), introduce negative supercoils (gyrase), or relax negative supercoils (TopA). If the DNA supercoils generated in the presence of cohesin-SMC1^{4E} and cohesin$^{EQ/EQ}$ are of opposite handedness, these plasmids should show differential sensitivity to these

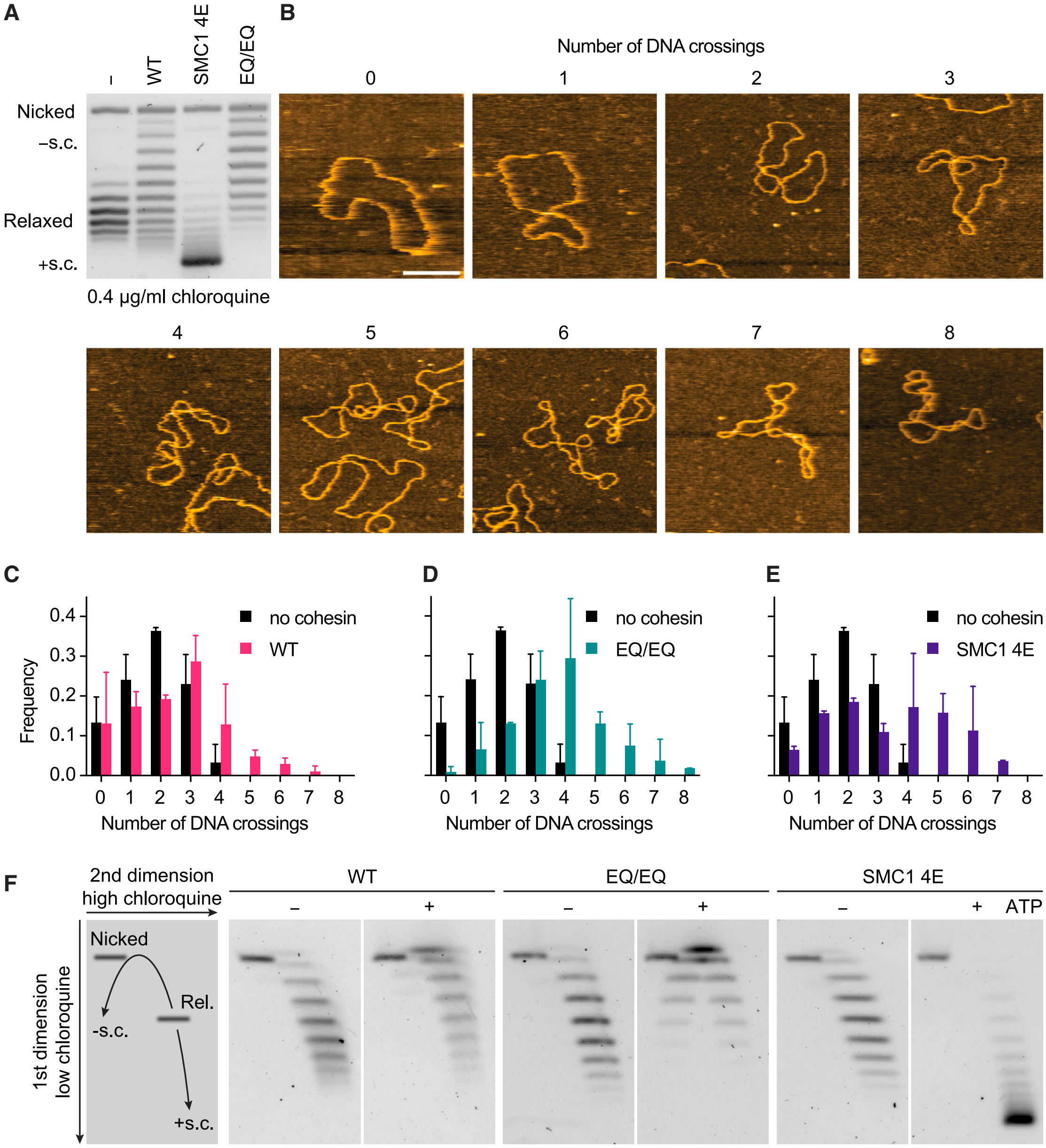

Figure 2. Visualization of supercoiled DNA by HS-AFM

(A) Plasmid supercoiling assay. Negatively supercoiled plasmid DNA was relaxed by incubating with human topoisomerase I and ATP. Reactions were then supplemented as indicated with cohesin (15:1 cohesin/plasmid ratio). NIPBL-MAU2 was added at a 2-fold molar excess relative to cohesin.

(B) Purified DNA from (A) was visualized using high-speed atomic force microscopy (HS-AFM). Images of plasmid DNA with the indicated number of DNA crossings. The images with 0–6 DNA crossings were recorded using the WT DNA sample shown in (A). The images with 7-8 DNA crossings were recorded using the EQ/EQ DNA sample shown in (A). Scale bar, 200 nm.

(C–E) Frequency of DNA crossings observed per DNA molecule by HS-AFM. Data are mean ± SD from two independent experiments. *N* = 102, 104, 108, and 108 plasmids analyzed per no cohesin, wild-type cohesin, cohesin-SMC1^{4E}, and cohesin$^{EQ/EQ}$ conditions, respectively.

(F) Two-dimensional agarose gel electrophoresis of human topoisomerase I plasmid supercoiling assay reactions in the presence or absence of the indicated proteins and ATP. Cohesin and NIPBL-MAU2 were added to all reactions at 15:1 and 30:1 protein/plasmid ratios, respectively. Electrophoresis was performed in the presence of 0.1 and 1 μg/mL chloroquine in the first and second dimensions, respectively. The cartoon shows the expected migration pattern of nicked, relaxed, negatively supercoiled, and positively supercoiled DNA. For one-dimensional electrophoresis of these samples, see Figure 3E (25 mM NaCl).
See also Figure S2.

enzymes. Indeed, all experiments performed with Topo IV, DNA gyrase, and TopA confirmed that plasmids become negatively supercoiled in the presence of cohesin$^{EQ/EQ}$ but positively supercoiled in the presence of cohesin-SMC1^{4E} (Figures S3A–S3E and STAR Methods).

Our observation that mutation of cohesin's DNA-clamping sites results in a switch from negative to positive supercoiling is reminiscent of the recent observation that plasmids become negatively supercoiled at low condensin-to-DNA ratios but positively supercoiled at high ratios.[26] We therefore tested whether a similar switch is observed when cohesin-to-plasmid ratios are increased. We indeed found that this is the case for wild-type cohesin (Figures S3F and S3G) but not for cohesin$^{EQ/EQ}$ (Figure S3G).

Because positively supercoiled plasmids are generated in the presence of high wild-type cohesin-to-DNA ratios and by cohesin-SMC1^{4E} at any ratio, we wondered whether cohesin-SMC1^{4E} is hyperactive in supercoiling, i.e., whether it mimics high wild-type cohesin-to-DNA ratios. If so, one might observe negative supercoiling when cohesin-SMC1^{4E} is incubated at low cohesin-to-plasmid ratios or for short periods of time. However, negatively supercoiled plasmids could be detected in neither dose-response (Figure S3H) nor time-course (Figures S3I and S3J) analyses of reactions containing cohesin-SMC1^{4E}, indicating that this mutant is not a hyperactive form of cohesin.

Cohesin-SMC1^{4E} generates a negative twist of -0.6 in each loop-extrusion step

The switch in supercoiling handedness observed with DNA-clamping mutants and at high cohesin-to-plasmid ratios could represent a change in the handedness of cohesin's supercoiling activity or could result from an indirect effect. To distinguish between these possibilities, we analyzed cohesin-SMC1^{4E} in a magnetic tweezers assay in which the degree of DNA twisting that occurs during individual loop-extrusion steps can be measured.[39] Cohesin-SMC1^{4E} was able to induce step-like DNA-shortening events in this assay (Figure 3A). This suggests that cohesin-SMC1^{4E} is able to carry out loop-extrusion steps, even though this mutant displayed only little extrusion activity in fluorescence microscopy assays (3% of wild type) and was thus previously considered to be unable to support loop extrusion.[12]

Importantly, in this magnetic tweezers assay, cohesin-SMC1^{4E} generated a negative twist of -0.63 ± 0.12 (mean ± SD) in each loop-extrusion step (Figures 3B–3D), a value that has the same handedness and degree of twist as observed in the presence of wild-type cohesin.[39] This suggests that the switch in supercoiling handedness does not represent a change in handedness with which cohesin-SMC1^{4E} supercoils DNA but instead is caused by an indirect effect in the plasmid supercoiling assay.

Simulations predict a switch in supercoiling handedness

To test whether this effect could be related to the fact that L_k in the plasmid supercoiling assay is altered by topoisomerase I and not by cohesin, we used Monte Carlo simulations to model plasmid supercoiling *in silico* based on a set of simple parameters (Table S1 and STAR Methods). Since the analysis of magnetic tweezers experiments suggests that cohesin can extrude negative supercoils into loops,[39] we based our simulations on this notion. We further reasoned that loop extrusion would cause differential changes in the supercoiling density in the extruded and the non-extruded segments of the plasmid (Figure S4A). Since every loop-extrusion step introduces the same degree of negative twist[39] and reels a similar amount of DNA into the loop,[19] the ratio of supercoils per DNA unit length, i.e., the supercoiling density, would initially remain constant in the growing DNA loop. In contrast, in the non-looped segment the supercoiling density would increase with every loop-extrusion step, since each of these will shorten the segment but simultaneously introduce compensatory positive twist.

Finally, we assumed that topoisomerase I binds to all parts of the plasmid equally well. In plasmids containing identical numbers of cohesin-induced negative supercoils and compensatory positive supercoils, topoisomerase I would therefore preferentially bind to and resolve negative supercoils if the negative supercoils were distributed over a larger fraction of the plasmid than the positive supercoils. The opposite would be true if positive supercoils were distributed over a larger fraction.

To simulate the behavior of cohesin$^{EQ/EQ}$ we modeled it as wild-type cohesin, except that cohesin$^{EQ/EQ}$ was only allowed to take a single loop-extrusion step, as experimentally observed.[39] Since cohesin-SMC1^{4E} is predicted to bind DNA with reduced affinity, we reasoned that this mutant would be able to resist less torque in the clamped state when DNA becomes supercoiled. Remarkably, we found that these simulations predicted a switch from negative to positive supercoiling exactly under the conditions we had experimentally observed (Figures S4B–S4H; Videos S3 and S4). For wild-type cohesin, negative supercoiling was observed at low cohesin-to-plasmid ratios but positive supercoiling at high ratios (Figure S4B). This effect was observed over a range of simulated cohesin off rates and topoisomerase I relaxation rates (Figures S4I and S4J).

This supports the notion that the observed switch in supercoiling handedness is an indirect effect of the plasmid supercoiling assay, as opposed to cohesin itself changing the handedness of its supercoiling activity at high cohesin-to-plasmid ratios and when the DNA-clamping sites are mutated.

Testable predictions of the supercoiling-during-clamping hypothesis

Our results so far indicated that cohesin negatively supercoils DNA during clamping and that clamp mutations indirectly cause a change in supercoiling handedness in plasmid assays. This hypothesis makes several testable predictions. One of these is that weakening electrostatic interactions in the DNA clamp should also reduce supercoiling and induce a switch in supercoiling handedness. Remarkably, increased salt concentrations were indeed sufficient to generate positively supercoiled plasmids in the presence of wild-type cohesin at low cohesin-to-plasmid ratios (Figure 3E, compare lanes 2 and 14). In contrast, neither cohesin$^{EQ/EQ}$ nor single EQ mutants (cohesin-SMC1^{EQ} and cohesin-SMC3^{EQ}) showed such a switch at increased salt conditions (Figures 3E and S4K).

If cohesin-SMC1^{4E} generates positively supercoiled plasmids by negatively supercoiling DNA, then limiting the activity of

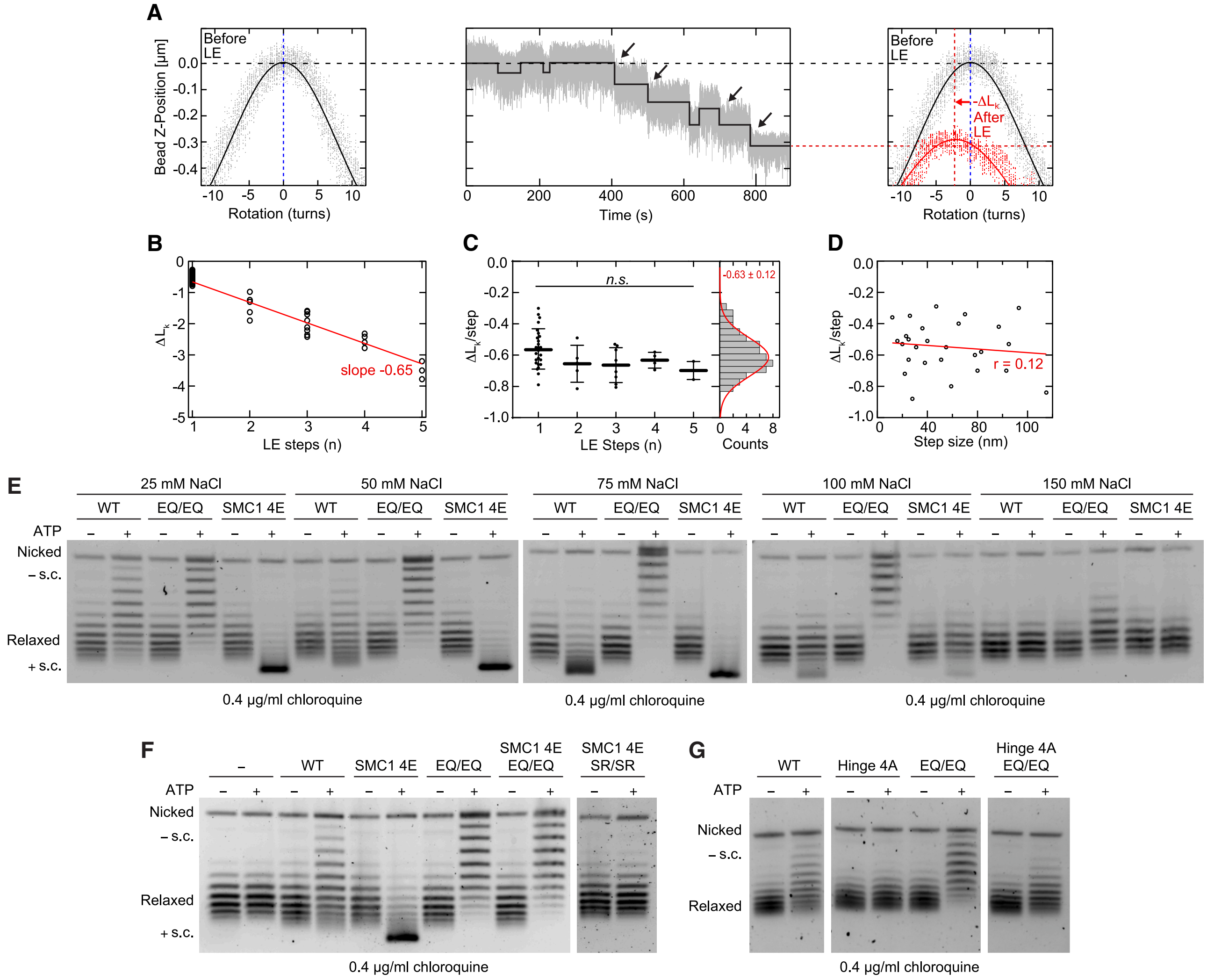

Figure 3. Individual cohesin-SMC1^{4E} steps introduce negative DNA twist

(A) (Left) End-to-end extension as a function of magnet rotation for a torsionally constrained 3.6 kb DNA. Extension at 0.3 pN force is maximal when no external rotations are applied. Upon applying positive/negative rotations, the over-/underwinding of the DNA changed the linking number L_k and led to the formation of supercoils, which are symmetric at this force. The solid line depicts a Gaussian fit to the rotation curve data. (Center) Representative trajectory of cohesin-SMC1^{4E} showing stepwise events in the presence of 1 mM ATP at 0.3 pN. The solid line depicts fit from the step-finding algorithm. (Right) DNA extension as a function of magnet rotation similar to panel on the left, conducted directly after the DNA loop-extrusion experiment. The rotation curve after loop extrusion (red; solid line depicts Gaussian fit to the data) shows that the maximum DNA extension was shifted to negative magnet rotation compared to the initial rotation curve (black), caused by the uncoiling of the positive complementary supercoils ($+\Delta L_k$) formed in the DNA molecule outside the DNA loop. The degree of negative supercoils ($-\Delta L_k$) generated by cohesin-SMC1^{4E} (red arrow) is equal to the degree of positive supercoils ($+\Delta L_k$) generated outside the loop.

(B) Change in DNA linking number, ΔL_k, over the indicated number of steps for cohesin-SMC1^{4E} in the presence of ATP (total $N = 54$). The red line represents a linear fit.

(C) The same data as in (B) but divided by the number of steps. The histogram on the right represents all data points, fitted by a Gaussian with -0.63 ± 0.12 turns (mean ± SD). Statistical significance was assessed using ANOVA with a significance level $\alpha = 0.05$ (95% confidence interval; n.s. [not significant], $p > 0.05$).

(D) Change in rotation per step is plotted against the step size for traces with only a single step ($N = 24$). Linear fit and Pearson's correlation coefficient are shown in red.

(E) Plasmid supercoiling assay at different NaCl concentrations. Negatively supercoiled plasmid DNA was relaxed by incubating with human topoisomerase I at the indicated NaCl concentrations. Reactions were then supplemented as indicated with ATP and cohesin at a 15:1 cohesin/plasmid ratio. NIPBL-MAU2 was added to all reactions at a 30:1 NIPBL-MAU2/plasmid ratio.

(F) As in (E), except cohesin and NIPBL-MAU2 were added to all reactions at a 20:1 and 40:1 protein/plasmid ratio, respectively in a buffer containing 25 mM NaCl.

(G) As in (E), except cohesin and NIPBL-MAU2 were added to all reactions at a 10:1 and 30:1 protein/plasmid ratio, respectively in a buffer containing 25 mM NaCl.

See also Figures S3 and S4.

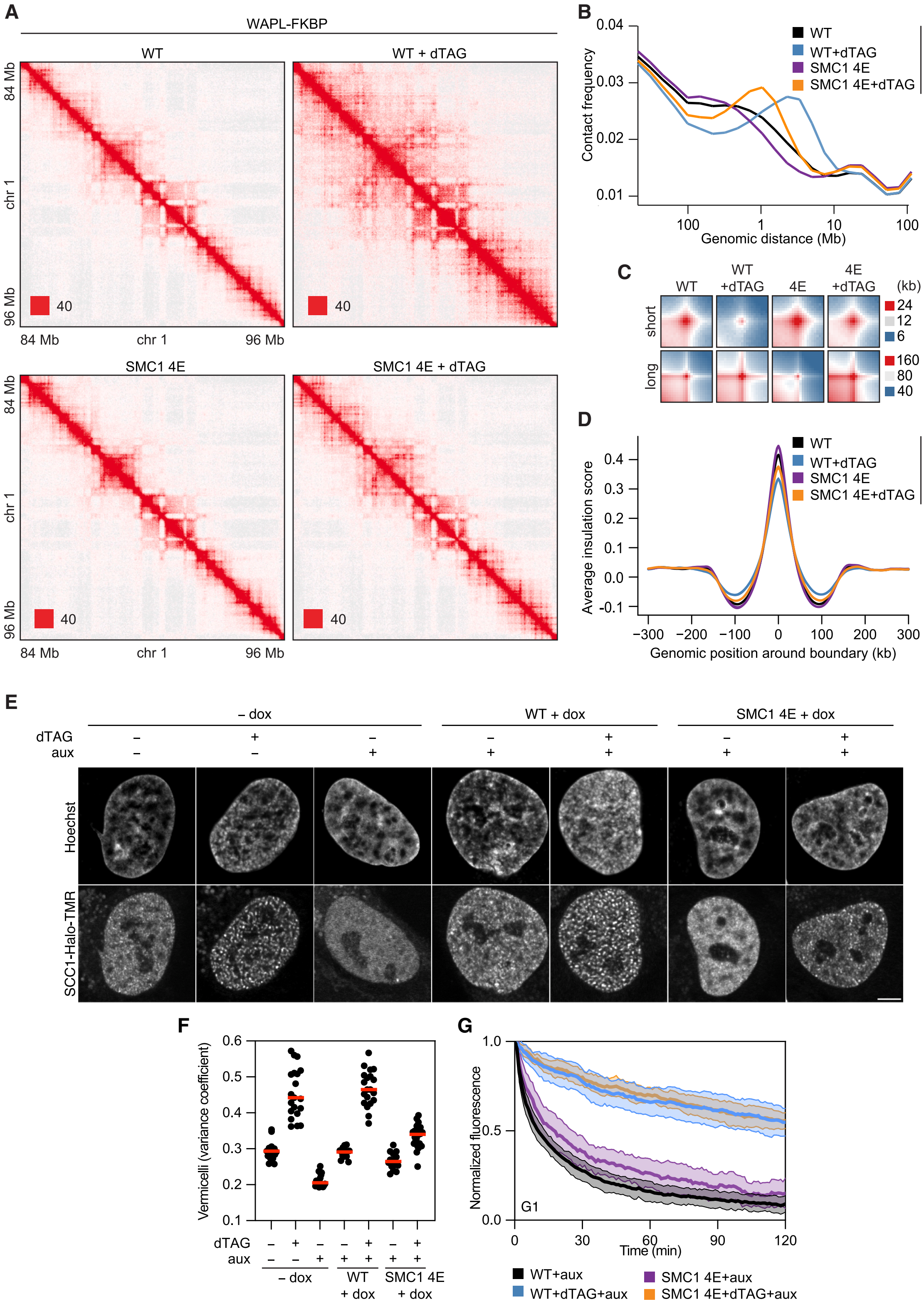

Figure 4. Cohesin-SMC1^{4E} forms shorter loops in cells

(A) Hi-C contact matrices of chromosome 1 (84–96 Mb) from cells treated with auxin to degrade endogenous SMC1, doxycycline to induce expression of wild-type SMC1 or SMC1^{4E}, and, where indicated, dTAG to degrade endogenous WAPL. Maximum intensity is indicated in the lower left of each panel.

(legend continued on next page)

cohesin-SMC1^{4E} to one step should reveal its negative supercoiling activity. Indeed, introducing EQ/EQ mutations into cohesin-SMC1^{4E} reverted its positive supercoiling activity back to negative supercoiling (Figure 3F). This epistatic effect was also predicted by our simulations (Figure S4E). In contrast, introducing the SR/SR mutations into cohesin-SMC1^{4E} greatly reduced supercoiling, supporting the hypothesis that supercoiling occurs upon head engagement and DNA clamping (Figure 3F). We also combined the EQ/EQ with the hinge^{4A} mutations, which reduce DNA binding at the hinge.[12] Little supercoiling could be detected in the presence of this cohesin$^{EQ/EQ}$-hinge^{4A} mutant, further supporting the notion that the hinge is also required for supercoiling (Figure 3G).

Cohesin-SMC1^{4E} forms shorter loops in cells

To test the effect of DNA-clamping deficiency on genome architecture in cells, we expressed either wild-type SMC1 or SMC1^{4E} from a doxycycline-inducible promoter in G_1-synchronized HeLa cells, depleted endogenous SMC1 by auxin-inducible degradation[42] (Figure S5A), and analyzed long-range chromosomal *cis* interactions by Hi-C. In cells expressing cohesin-SMC1^{4E}, long-range interactions were reduced genome wide and long corner peaks (chromatin loops) were reduced, whereas short-range interactions and short corner peaks were increased (Figures 4A–4C), although SMC1^{4E} associated with chromatin similarly well as wild-type SMC1 (Figure S5A). TAD numbers were not changed (Figure S5B), but interestingly the total number of corner peaks and TAD insulation were slightly increased in the presence of cohesin-SMC1^{4E} (Figures 4D and S5C), implying that cohesin-SMC1^{4E} stalls more frequently at CTCF sites than wild-type cohesin.

To test whether these phenotypes are caused by increased sensitivity of cohesin-SMC1^{4E} to the cohesin release factor WAPL,[43] we induced degradation of FKBP-tagged WAPL in these cells by dTAG (Figure S5A). This increased long-range interactions (Figures 4A and 4B) and reduced TAD insulation (Figure 4D), but not to the extent seen in the presence of wild-type SMC1. It also failed to restore the pattern of short and long corner peaks observed in the presence of wild-type SMC1 (Figure 4C). The observation that WAPL depletion does not fully restore the Hi-C phenotypes associated with SMC1^{4E} indicates that cohesin-SMC1^{4E} is not hypersensitive to release by WAPL but instead causes the above Hi-C phenotypes by defects in DNA clamping, negative supercoiling, and extrusion.

WAPL depletion increases the processivity of cohesin-mediated loop extrusion.[4,44] This results in a dramatic relocalization of cohesin from most chromatin regions to axial chromosomal “vermicelli” domains, which represent the base of cohesin loops.[45] We therefore used vermicelli formation as an orthogonal assay to test whether cohesin-SMC1^{4E} can perform loop extrusion as well as wild-type cohesin. Fluorescence microscopy of WAPL-depleted cells expressing SMC1^{4E} revealed that much less cohesin accumulated in vermicelli compared to cells expressing wild-type SMC1 (Figures 4E and 4F). These results further support the notion that cohesin-SMC1^{4E} is reduced in its ability to form long chromatin loops.

We next analyzed whether cohesin-SMC1^{4E} forms shorter chromatin loops and less intense vermicelli because its residence time on chromatin is reduced. However, inverse fluorescence recovery after photobleaching (iFRAP) experiments revealed that cohesin-SMC1^{4E} had a slightly longer chromatin residence time than wild-type cohesin, and WAPL degradation stabilized wild-type and SMC1^{4E} on chromatin to a similar extent (Figures 4G, S5D, and S5E). Thus, the shorter chromatin loops observed in the presence of cohesin-SMC1^{4E} are not caused by a reduction in the chromatin residence time of cohesin-SMC1^{4E}.

Since the total number of corner peaks and TAD insulation were increased in the presence of cohesin-SMC1^{4E} (Figures 4D and S5C), we wondered whether cohesin-SMC1^{4E} forms shorter chromatin loops only because it stops more frequently at CTCF sites than wild-type cohesin. To test this possibility, we analyzed chromatin loops formed by cohesin-SMC1^{4E} in cells depleted of both WAPL and CTCF (Figures 5 and S5F). However, also in the absence of both WAPL and CTCF, cohesin-SMC1^{4E} formed shorter chromatin loops than wild-type cohesin (Figures 5A–5D). These results indicate that cohesin-SMC1^{4E} forms shorter chromatin loops not only because it stalls more frequently at CTCF sites but also because its DNA-clamping, negative supercoiling, and loop-extrusion activities are reduced.

Our observations therefore indicate that cohesin’s DNA-clamping and negative supercoiling activities are required for DNA loop extrusion not only *in vitro* but also for chromatin looping in cells. These data further imply that the strength of TAD boundaries depends on cohesin’s loop-extruding activity. If this activity is reduced, as in cohesin-SMC1^{4E}, these boundaries become stronger (Figures 4D and S5C), but if this activity is increased, as seen in WAPL-depleted cells, TAD boundaries become weaker (Figure 4D).[4,44]

(B) Intra-chromosomal Hi-C contact frequency distribution plotted as a function of genomic distance in cells treated as described in (A).

(C) Aggregated Hi-C peak analysis from cells as described in (A). Short: chromatin loops >100 kb at coordinates identified in SCC1-GFP HeLa cells. Long: chromatin loops >500 kb at coordinates identified in auxin-treated WAPL-AID HeLa cells.

(D) Average insulation score around TAD boundaries in cells as described in (A).

(E) Representative live cell images of SCC1-HaloTMR in cells treated with auxin, dTAG, and doxycycline as indicated to degrade endogenous SMC1, degrade endogenous WAPL, and induce expression of wild-type SMC1 or SMC1^{4E}, respectively. DNA was stained with Hoechst. Scale bar, 5 μm.

(F) Quantification of vermicelli by measuring the coefficient variation of SCC1-HaloTMR fluorescence intensity (red bar denotes mean; data points are from individual cells obtained from three independent experiments). *N* = 20, 21, 19, 14, 20, 14, and 22 cells per condition, ordered left to right as displayed.

(G) Normalized recovery kinetics of SCC1-HaloTMR signals after photobleaching of cohesin-WT and cohesin-SMC1^{4E} cells in G_1 phase treated with auxin as indicated to degrade endogenous WAPL (mean ± SD). *N* = 12 (WT + aux), 12 (WT + dTAG + aux), 13 (SMC1 4E + aux), and 12 (SMC1 4E + dTAG + aux) cells. For representative images, see Figure S5D.

See also Figure S5.

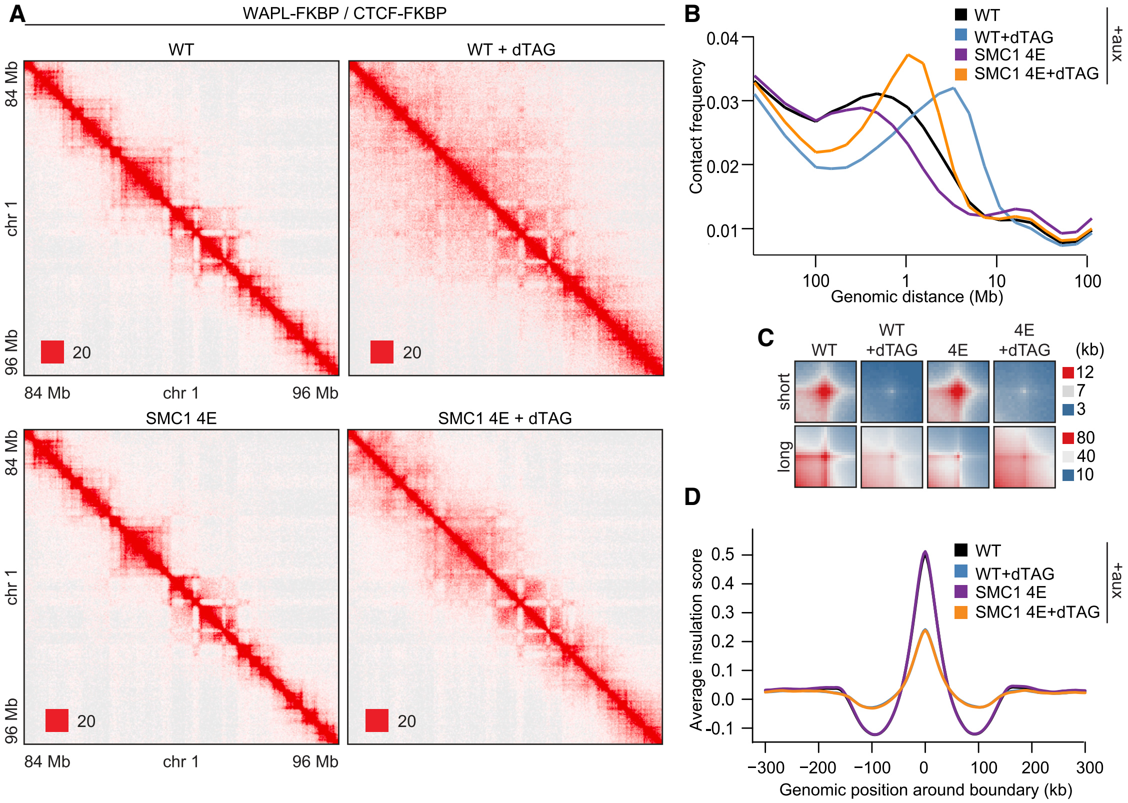

Figure 5. Cohesin-SMC1^{4E} forms shorter genomic contacts in cells also in the absence of CTCF

(A) Hi-C contact matrices of chromosome 1 (84–96 Mb) from cells treated with auxin to degrade endogenous SMC1, doxycycline to induce expression of wild-type SMC1 or SMC1^{4E}, and, where indicated, dTAG to degrade endogenous WAPL and CTCF. Maximum intensity is indicated in the lower left of each panel.

(B) Intra-chromosomal Hi-C contact frequency distribution plotted as a function of genomic distance in cells treated as described in (A).

(C) Aggregated Hi-C peak analysis from cells as described in (A). Short: chromatin loops >100 kb at coordinates identified in SCC1-GFP HeLa cells. Long: chromatin loops >500 kb at coordinates identified in auxin-treated WAPL-AID HeLa cells.

(D) Average insulation score around TAD boundaries in cells as described in (A).

See also Figure S5.

Topoisomerase I facilitates the formation of chromatin loops by cohesin

If cohesin extrudes negative supercoils into loops, as has been suggested,[39] topoisomerases might be required to resolve these supercoils. A role for topoisomerases in the formation of cohesin loops has already been proposed based on the analysis of vermicelli in cells treated with topoisomerase I and II inhibitors.[46] However, these inhibitors not only reduced the frequency of cells forming vermicelli but also induced chromatin compaction, making it difficult to distinguish between direct and indirect effects of topoisomerase inhibition on vermicelli formation.

We therefore generated cell lines in which topoisomerase I (TOP1) or topoisomerases IIA and IIB (TOP2AB) could be depleted, either alone or together with WAPL (Figures S5G–S5I) and analyzed vermicelli formation in these cells (Figures 6A and 6B). Depletion of topoisomerases IIA and IIB showed only a small and non-significant reduction in vermicelli (Figures 6B and 6C). However, depletion of topoisomerase I reduced vermicelli formation significantly (Figures 6A and 6C). Importantly, neither topoisomerase I nor topoisomerase IIA/IIB depletion induced chromatin compaction, consistent with the possibility that the effect of topoisomerase I depletion on vermicelli is direct.

We therefore analyzed cells depleted of topoisomerase I by Hi-C. In these cells, short chromatin loops were not detectably reduced (Figures 6D–6G and S5J–S5L). However, long chromatin loops, particularly those seen following depletion of WAPL, were reproducibly reduced in abundance (Figures 6D–6G). In contrast, compartmentalization was increased in these cells (Figure 6H), presumably as a result of reduced chromatin looping by cohesin, which is known to suppress compartmentalization.[2–4,47,48] These results indicate that topoisomerase I is required for the formation of long chromatin loops by cohesin.

DISCUSSION

Our results show that cohesin supercoils DNA and indicate that this activity is an integral part of the loop-extrusion process. Our data and magnetic tweezers experiments by Janissen et al. reveal that negative supercoiling is a universal feature of all eukaryotic SMC complexes.[39] These findings expand earlier observations that condensin supercoils DNA[24–26] and are consistent with the observation that oligonucleotides bound to the *E. coli* SMC complex MukBEF are oriented as if they represent parts of a negatively supercoiled loop.[49] These findings provide fundamental insight into the mechanism of DNA loop extrusion, have important implications for the regulation of genome architecture, and suggest that supercoiling is a common feature of SMC-mediated genome folding in all kingdoms of life.

Key steps in the loop-extrusion cycle are the ATP-driven engagement of cohesin's ATPase heads, resulting in ∼15 pN force generation,[18] DNA translocation (∼100–200 bp/step[19,50]), and subsequent DNA clamping. Our results indicate that cohesin supercoils DNA during these steps, implying that head engagement and force generation are used not only to translocate DNA but also to twist it. Our finding that DNA-binding sites in the clamp and at the hinge are needed for supercoiling suggests that this process occurs when DNA is constrained between the hinge and the clamp. Since cohesin's coiled coils can twist around each other,[12] it will be interesting to test whether supercoiling depends on or promotes these coiled-coil movements.

Our plasmid supercoiling experiments cannot directly distinguish between multiple supercoils being introduced into a plasmid by a single cohesin, as opposed to plasmids being bound by multiple cohesin complexes each introducing some twist. The latter situation must occur in the presence of cohesin$^{EQ/EQ}$, since this mutant is unable to hydrolyze ATP and can thus only clamp but not extrude DNA. However, several observations suggest that wild-type cohesin can introduce multiple supercoils into plasmids during successive ATP binding-hydrolysis and loop-extrusion cycles. First, magnetic tweezers experiments suggest that wild-type cohesin can twist DNA during successive loop-extrusion steps, whereas cohesin$^{EQ/EQ}$ can only induce a single step of DNA twisting.[39] Second, our Monte Carlo simulations can explain the generation of positively supercoiled plasmids in the presence of high cohesin-to-DNA ratios if one assumes that one cohesin molecule can generate multiple supercoils (Figure S4). The notion that a single wild-type cohesin complex can generate multiple supercoils, whereas cohesin$^{EQ/EQ}$ cannot, is also supported by our observation that these complexes display different behaviors at elevated ionic strength or when their ratio to DNA is increased. In the presence of wild-type cohesin this results in a switch to positive supercoiling, but in the presence of cohesin$^{EQ/EQ}$ such a switch is never observed (Figures 3E, S3G, and S4K), indicating that these two forms of cohesin supercoil plasmids differently.

Although condensin's supercoiling activity was discovered almost three decades ago,[25] it has never been tested whether this activity is required in cells. Our observation that cohesin mutated in one of the clamp's DNA-binding sites[12] (cohesin-SMC1^{4E}) is defective in negative supercoiling *in vitro* and forms shorter genomic contacts in cells implies that cohesin's ability to supercoil DNA is indeed important for chromatin looping in cells. An interesting corollary of this conclusion is that SMC-dependent genomic contacts detected by Hi-C might represent not only loops but also supercoiled DNA, such as plectonemic structures.

However, since cohesin-SMC1^{4E} is not only defective in negative supercoiling but also reduced in its *in vitro* loop-extrusion activity,[12] the Hi-C phenotype caused by this mutant could be due to defects either in supercoiling or in loop extrusion. Although we can formally not distinguish between these possibilities, we suspect that both of these reasons are true, since our data suggest that supercoiling is an integral part of the loop-extrusion process.

Unexpectedly, cohesin-SMC1^{4E} causes a much more severe phenotype during loop extrusion *in vitro*[12] than in cells (Figure 4). Based on similar observations made in yeast, it has been proposed that chromatin loops in cells are not formed by loop extrusion.[51] However, this interpretation cannot explain key features of chromatin loops and cohesin in cells, such as the CTCF convergence rule[52–56] and vermicelli formation after WAPL depletion.[45,53] We therefore favor the interpretation that cohesin-SMC1^{4E} causes phenotypes of different severities in cells and in *in vitro* assays because these differ greatly with respect to the conditions under which cohesin-SMC1^{4E} functions. For example, in cells cohesin-SMC1^{4E} has to form loops in the presence of WAPL, whereas in our *in vitro* loop-extrusion assay WAPL is absent. It is therefore conceivable that in cells the apparent chromatin looping activities of wild-type cohesin and cohesin-SMC1^{4E} are not as different as *in vitro*, since the loop-extrusion activity of wild-type cohesin is dampened by WAPL in cells. Consistent with this possibility, we find that WAPL depletion reveals a much bigger difference between the chromatin looping activities of wild-type cohesin and cohesin-SMC1^{4E} in cells (Figure 4).

Cohesin and condensin are sensitive to DNA tension, halting loop extrusion once a certain stall force has been reached,[19,57] and the ability of the barrier protein CTCF to block cohesin-mediated loop extrusion increases with DNA tension.[19] Our observation that cohesin supercoils DNA therefore raises the interesting possibility that this sensitivity may not be restricted to linear force but that cohesin might also be sensitive to forces that occur when DNA becomes twisted, i.e., to torque. According to this hypothesis, cohesin-SMC1^{4E} might be defective in negative supercoiling *in vitro* and in forming long chromatin loops in cells because it has a reduced stall torque. This stall torque would depend on the DNA-binding affinity of the clamp, which is reduced in cohesin-SMC1^{4E}. Our Monte Carlo simulations support this notion, since the unusual behavior of cohesin-SMC1^{4E} in plasmid assays, in which it generates positively supercoiled DNA in the presence of topoisomerase I, can be simulated simply by assuming that this mutant has a reduced stall torque (Figure S4D). It is therefore conceivable that loop-extrusion-induced torque at CTCF sites contributes to its barrier activity and may explain why Hi-C contacts are particularly enriched at these positions upon expression of SMC1^{4E} (Figure 4C).

This hypothesis raises the interesting possibility that topoisomerases might be required to prevent stalling of SMC complexes, which otherwise would stop extruding DNA once they had reached their stall torque. This hypothesis could explain why topoisomerases accumulate at the base of cohesin and condensin loops[20–23,29–33] and, conversely, why cohesin accumulates at active genes, which are known to accumulate supercoils.[58] Consistent with this possibility, we observed that depletion of topoisomerase I reduced vermicelli formation and the abundance of long chromatin loops in cells. Similarly, depletion of topoisomerase II has been found to reduce the formation of chromatin loops by the condensin-related dosage

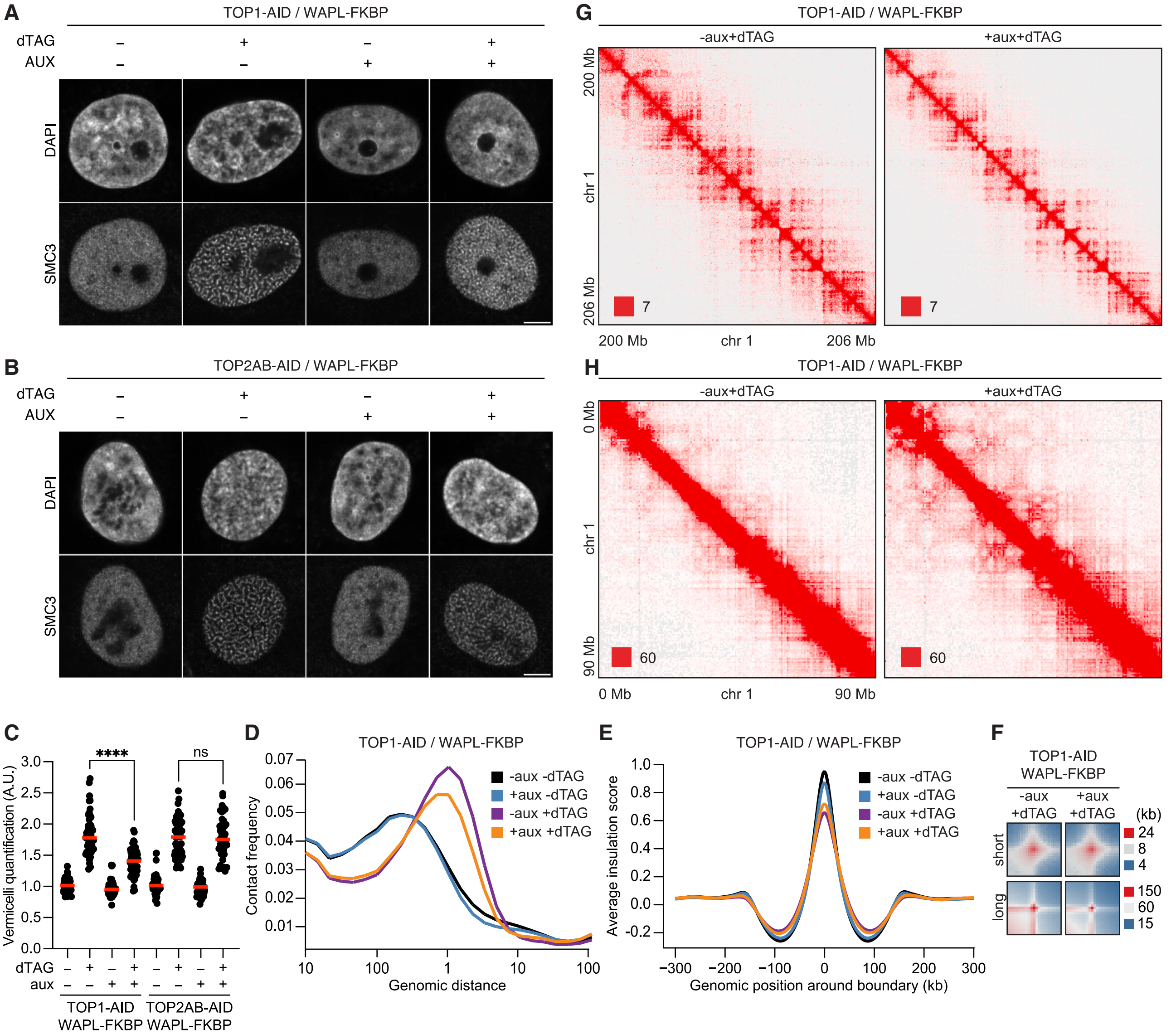

Figure 6. Topoisomerase I facilitates the formation of vermicelli and long-range chromatin contacts that occur upon depletion of WAPL

(A and B) Representative SMC3 immunofluorescence microscopy images from (A) topoisomerase I (TOP1)-AID/WAPL-FKBP and (B) topoisomerases IIA and IIB (TOP2AB)-AID/WAPL-FKBP HeLa cells treated as indicated with dTAG to degrade endogenous WAPL or auxin to degrade endogenous TOP1 or TOP2A and TOP2B in combination, respectively. DNA was stained with DAPI. Scale bar, 5 μm.

(C) Quantification of vermicelli in cells treated as described in (A) and (B) by measuring the inter-vermicelli distance (red bar denotes median; data points are from individual cells obtained from two independent experiments). *N* = 49, 55, 46, 58, 50, 54, 43, and 40 cells analyzed per condition, ordered left to right as displayed. Statistical significance was determined using a Mann-Whitney test. $^{****}p < 0.0001$; ns (not significant), $p > 0.5$.

(D) Intra-chromosomal Hi-C contact frequency distribution plotted as a function of genomic distance in TOP1-AID/WAPL-FKBP HeLa cells treated with dTAG and auxin as indicated.

(E) Average insulation score around TAD boundaries in cells as described in (D).

(F) Aggregated Hi-C peak analysis. Short: chromatin loops >100 kb at coordinates identified in SCC1-GFP HeLa cells. Long: chromatin loops >500 kb at coordinates identified in auxin-treated WAPL-AID HeLa cells.

(G and H) Hi-C contact matrices of chromosome 1 (G: 200–206 Mb; H: 0–90 Mb) from TOP1-AID/WAPL-FKBP HeLa cells treated with dTAG and auxin as indicated. Maximum intensity is indicated in the lower left of each panel. For non-dTAG-treated matrices, see Figure S5K.

See also Figure S5.

compensation complex in *C. elegans*.[59] In our experiments, the effect of topoisomerase I depletion on the formation of long chromatin loops was mild, but the effect size in this experiment could be limited by functional redundancy between type I and II topoisomerases. In future experiments it will therefore be important to analyze the effect of simultaneous depletion of all nuclear topoisomerases on cohesin-mediated chromatin looping. Likewise, it will be interesting to test whether topoisomerases are required for protocadherin promoter choice[5] and immunoglobulin gene recombination[6,7] because these processes depend on the formation of particularly long chromatin loops by cohesin.

Limitations of the study

Our experiments do not directly address whether cohesin twists DNA transiently, as has been proposed for condensin,[26] or adds twist into the loop with every extrusion step, as has been concluded from magnetic tweezers experiments.[39] However, we note that our Monte Carlo simulations and Hi-C analysis of topoisomerase I-depleted cells are consistent with the latter. Our experiments also cannot distinguish between topoisomerase I enabling the formation of chromatin loops by resolving supercoils generated by transcription or by cohesin. More work will be needed to test these possibilities, which are not mutually exclusive.

RESOURCE AVAILABILITY

Lead contact

Requests for further information and resources should be directed to and will be fulfilled by the lead contact, Jan-Michael Peters (peters@imp.ac.at).

Materials availability

All plasmids and cell lines generated in this study are available from the lead contact with a completed materials transfer agreement.

Data and code availability

- Sequencing data have been deposited in the Gene Expression Omnibus under accession number GEO: GSE292596.
- All original code can be downloaded at 4TU.ResearchData: https://data.4tu.nl/private_datasets/2V3F14Y-Y2A3XQEf9EN6Pj7o6pXaTL2m62-LCX5Ng9w.
- Any additional information required to reanalyze the data reported in this paper is available from the lead contact upon request.

ACKNOWLEDGMENTS

We thank Thomas Lendl (IMBA/IMP/GMI BioOptics) for assistance with vermicelli quantification, staff at IMBA/IMP/GMI BioOptics, Molecular Biology Service and Next-Generation Sequencing for technical support, Daniela Goetz for cloning wild-type trimeric cohesin, and all Peters and Dekker lab members for discussions. We acknowledge the use of computational resources of the DelftBlue supercomputer, provided by the Delft High Performance Computing Center (https://www.tudelft.nl/dhpc). J.-M.P. is also an adjunct professor at the Medical University of Vienna. Research in the laboratory of C.D. is supported by European Research Council advanced grant 883684 (DNA looping), NWO grant OCENW.GROOT.2019.012, and the BaSyC Program. Research in the laboratory of J.-M.P. is supported by Boehringer Ingelheim, the Austrian Life Sciences Programme 2023 (LS23 IF, project FO999902549), the European Research Council Horizon 2020 Research and Innovation Programme 101020558, the Human Frontier Science Program RGP0057/2018, and the Vienna Science and Technology Fund LS19-029.

AUTHOR CONTRIBUTIONS

I.F.D., K.N., W.T., G.W., R.B., S.H., R.J., E.C., C.D., and J.-M.P. designed experiments. I.F.D. generated constructs for protein expression, purified proteins, performed plasmid supercoiling experiments, and analyzed data. K.N. generated HeLa cell SMC1 expression constructs and cell lines and performed and analyzed cellular experiments in which expression of SMC1^{WT} and SMC1^{4E} were compared. W.T. generated TOP1-AID/WAPL-FKBP and TOP2AB-AID/WAPL-FKBP HeLa cell lines and performed and analyzed cellular experiments using these cell lines. G.W. purified human topoisomerase I and generated Hi-C libraries. R.B. and R.J. performed magnetic tweezers experiments. R.J. analyzed magnetic tweezers data. R.B. performed simulations. S.H. performed high-speed atomic force microscopy and analyzed data. R.R.S. analyzed Hi-C data. E.C. generated constructs for protein expression, purified proteins, and performed SMC1^{EEEG}, single EQ cohesin, and hinge 4A/EQ/EQ plasmid supercoiling experiments. B.W.B. generated cohesin ATPase head and hinge DNA-binding mutants, SMC1^{EEEG}, and single-chain cohesin constructs. I.F.D. and J.-M.P. wrote the manuscript with input from all authors. J.-M.P. and C.D. supervised the study.

DECLARATION OF INTERESTS

The authors declare no competing interests.

STAR★METHODS

Detailed methods are provided in the online version of this paper and include the following:

- KEY RESOURCES TABLE
- EXPERIMENTAL MODEL AND STUDY PARTICIPANT DETAILS
- METHOD DETAILS
  - Cloning and mutagenesis
  - Protein expression
  - Cohesin and NIPBL-MAU2 purification
  - Single-chain trimeric cohesin purification
  - STAG1 purification
  - PDS5A purification
  - Human topoisomerase I purification
  - Human topoisomerase I plasmid supercoiling assay
  - Single-chain cohesin plasmid supercoiling assay
  - Pre-relaxed plasmid supercoiling assay
  - Supercoiling handedness experiments
  - Two-dimensional agarose gel electrophoresis
  - High-speed atomic force microscopy
  - Magnetic tweezers experiments
  - Cell extracts and western blotting
  - Hi-C library preparation
  - Vermicelli imaging and pciFRAP
- QUANTIFICATION AND STATISTICAL ANALYSIS
  - High-speed atomic force microscopy analysis
  - Magnetic tweezers analyses
  - 1D cohesin supercoiling simulations
  - Hi-C data processing
  - Vermicelli quantification
  - pciFRAP analysis and curve fitting

SUPPLEMENTAL INFORMATION

Supplemental information can be found online at https://doi.org/10.1016/j.celrep.2025.115856.

Received: December 2, 2024
Revised: March 19, 2025
Accepted: May 27, 2025

REFERENCES

1. Gassler, J., Brandão, H.B., Imakaev, M., Flyamer, I.M., Ladstätter, S., Bickmore, W.A., Peters, J.M., Mirny, L.A., and Tachibana, K. (2017). A mechanism of cohesin-dependent loop extrusion organizes zygotic genome architecture. EMBO J. *36*, 3600–3618. https://doi.org/10.15252/embj.201798083.

2. Rao, S.S.P., Huang, S.C., Glenn St Hilaire, B., Engreitz, J.M., Perez, E.M., Kieffer-Kwon, K.R., Sanborn, A.L., Johnstone, S.E., Bascom, G.D., Bochkov, I.D., et al. (2017). Cohesin Loss Eliminates All Loop Domains. Cell (Cambridge, MA, U. S.) *171*, 305–320.e24. https://doi.org/10.1016/j.cell.2017.09.026.
3. Schwarzer, W., Abdennur, N., Goloborodko, A., Pekowska, A., Fudenberg, G., Loe-Mie, Y., Fonseca, N.A., Huber, W., Haering, C.H., Mirny, L., and Spitz, F. (2017). Two independent modes of chromatin organization revealed by cohesin removal. Nature (London) *551*, 51–56. https://doi.org/10.1038/nature24281.
4. Wutz, G., Várnai, C., Nagasaka, K., Cisneros, D.A., Stocsits, R.R., Tang, W., Schoenfelder, S., Jessberger, G., Muhar, M., Hossain, M.J., et al. (2017). Topologically associating domains and chromatin loops depend on cohesin and are regulated by CTCF, WAPL, and PDS5 proteins. EMBO J. *36*, 3573–3599. https://doi.org/10.15252/embj.201798004.
5. Kiefer, L., Chiosso, A., Langen, J., Buckley, A., Gaudin, S., Rajkumar, S. M., Servito, G.I.F., Cha, E.S., Vijay, A., Yeung, A., et al. (2023). WAPL functions as a rheostat of Protocadherin isoform diversity that controls neural wiring. Science. *380*, eadf8440. https://doi.org/10.1126/science.adf8440.
6. Hill, L., Ebert, A., Jaritz, M., Wutz, G., Nagasaka, K., Tagoh, H., Kostanova-Poliakova, D., Schindler, K., Sun, Q., Bönelt, P., et al. (2020). Wapl repression by Pax5 promotes V gene recombination by Igh loop extrusion. Nature (London) *584*, 142–147. https://doi.org/10.1038/s41586-020-2454-y.
7. Zhang, Y., Zhang, X., Ba, Z., Liang, Z., Dring, E.W., Hu, H., Lou, J., Kyritsis, N., Zurita, J., Shamim, M.S., et al. (2019). The fundamental role of chromatin loop extrusion in physiological V(D)J recombination. Nature (London) *573*, 600–604. https://doi.org/10.1038/s41586-019-1547-y.
8. Batty, P., Langer, C.C., Takács, Z., Tang, W., Blaukopf, C., Peters, J.M., and Gerlich, D.W. (2023). Cohesin-mediated DNA loop extrusion resolves sister chromatids in G2 phase. EMBO J. *42*, e113475. https://doi.org/10.15252/embj.2023113475.
9. Emerson, D.J., Zhao, P.A., Cook, A.L., Barnett, R.J., Klein, K.N., Saulebekova, D., Ge, C., Zhou, L., Simandi, Z., Minsk, M.K., et al. (2022). Cohesin-mediated loop anchors confine the locations of human replication origins. Nature (London) *606*, 812–819. https://doi.org/10.1038/s41586-022-04803-0.
10. Davidson, I.F., Bauer, B., Goetz, D., Tang, W., Wutz, G., and Peters, J.M. (2019). DNA loop extrusion by human cohesin. Science. *366*, 1338–1345. https://doi.org/10.1126/science.aaz3418.
11. Kim, Y., Shi, Z., Zhang, H., Finkelstein, I.J., and Yu, H. (2019). Human cohesin compacts DNA by loop extrusion. Science. *366*, 1345–1349. https://doi.org/10.1126/science.aaz4475.
12. Bauer, B.W., Davidson, I.F., Canena, D., Wutz, G., Tang, W., Litos, G., Horn, S., Hinterdorfer, P., and Peters, J.M. (2021). Cohesin mediates DNA loop extrusion by a "swing and clamp" mechanism. Cell (Cambridge, MA, U. S.) *184*, 5448–5464.e22. https://doi.org/10.1016/j.cell.2021.09.016.
13. Dekker, C., Haering, C.H., Peters, J.M., and Rowland, B.D. (2023). How do molecular motors fold the genome? Science. *382*, 646–648. https://doi.org/10.1126/science.adi8308.
14. Hopfner, K.P., Karcher, A., Shin, D.S., Craig, L., Arthur, L.M., Carney, J.P., and Tainer, J.A. (2000). Structural biology of Rad50 ATPase: ATP-driven conformational control in DNA double-strand break repair and the ABC-ATPase superfamily. Cell (Cambridge, MA, U. S.) *101*, 789–800. https://doi.org/10.1016/s0092-8674(00)80890-9.
15. Collier, J.E., Lee, B.-G., Roig, M.B., Yatskevich, S., Petela, N.J., Metson, J., Voulgaris, M., Gonzalez Llamazares, A., Löwe, J., and Nasmyth, K.A. (2020). Transport of DNA within cohesin involves clamping on top of engaged heads by Scc2 and entrapment within the ring by Scc3. eLife *9*, e59560. https://doi.org/10.7554/eLife.59560.
16. Higashi, T.L., Eickhoff, P., Sousa, J.S., Locke, J., Nans, A., Flynn, H.R., Snijders, A.P., Papageorgiou, G., O'Reilly, N., Chen, Z.A., et al. (2020). A Structure-Based Mechanism for DNA Entry into the Cohesin Ring. Mol. Cell *79*, 917–933.e9.
17. Shi, Z., Gao, H., Bai, X.C., and Yu, H. (2020). Cryo-EM structure of the human cohesin-NIPBL-DNA complex. Science. *368*, 1454–1459.
18. Pobegalov, G., Chu, L.Y., Peters, J.M., and Molodtsov, M.I. (2023). Single cohesin molecules generate force by two distinct mechanisms. Nat. Commun. *14*, 3946. https://doi.org/10.1038/s41467-023-39696-8.
19. Davidson, I.F., Barth, R., Zaczek, M., van der Torre, J., Tang, W., Nagasaka, K., Janissen, R., Kerssemakers, J., Wutz, G., Dekker, C., and Peters, J.M. (2023). CTCF is a DNA-tension-dependent barrier to cohesin-mediated loop extrusion. Nature (London) *616*, 822–827. https://doi.org/10.1038/s41586-023-05961-5.
20. Canela, A., Maman, Y., Huang, S.Y.N., Wutz, G., Tang, W., Zagnoli-Vieira, G., Callen, E., Wong, N., Day, A., Peters, J.M., et al. (2019). Topoisomerase II-Induced Chromosome Breakage and Translocation Is Determined by Chromosome Architecture and Transcriptional Activity. Mol. Cell *75*, 252–266.e8. https://doi.org/10.1016/j.molcel.2019.04.030.
21. Canela, A., Maman, Y., Jung, S., Wong, N., Callen, E., Day, A., Kieffer-Kwon, K.R., Pekowska, A., Zhang, H., Rao, S.S.P., et al. (2017). Genome Organization Drives Chromosome Fragility. Cell (Cambridge, MA, U. S.) *170*, 507–521.e18. https://doi.org/10.1016/j.cell.2017.06.034.
22. Gothe, H.J., Bouwman, B.A.M., Gusmao, E.G., Piccinno, R., Petrosino, G., Sayols, S., Drechsel, O., Minneker, V., Josipovic, N., Mizi, A., et al. (2019). Spatial Chromosome Folding and Active Transcription Drive DNA Fragility and Formation of Oncogenic MLL Translocations. Mol. Cell *75*, 267–283.e12. https://doi.org/10.1016/j.molcel.2019.05.015.
23. Uusküla-Reimand, L., Hou, H., Samavarchi-Tehrani, P., Rudan, M.V., Liang, M., Medina-Rivera, A., Mohammed, H., Schmidt, D., Schwalie, P., Young, E.J., et al. (2016). Topoisomerase II beta interacts with cohesin and CTCF at topological domain borders. Genome Biol. *17*, 182. https://doi.org/10.1186/s13059-016-1043-8.
24. Kim, E., Gonzalez, A.M., Pradhan, B., van der Torre, J., and Dekker, C. (2022). Condensin-driven loop extrusion on supercoiled DNA. Nat. Struct. Mol. Biol. *29*, 719–727. https://doi.org/10.1038/s41594-022-00802-x.
25. Kimura, K., and Hirano, T. (1997). ATP-dependent positive supercoiling of DNA by 13S condensin: a biochemical implication for chromosome condensation. Cell (Cambridge, MA, U. S.) *90*, 625–634. https://doi.org/10.1016/s0092-8674(00)80524-3.
26. Martínez-García, B., Dyson, S., Segura, J., Ayats, A., Cutts, E.E., Gutierrez-Escribano, P., Aragón, L., and Roca, J. (2023). Condensin pinches a short negatively supercoiled DNA loop during each round of ATP usage. EMBO J. *42*, e111913. https://doi.org/10.15252/embj.2022111913.
27. Baxter, J., Sen, N., Martínez, V.L., De Carandini, M.E.M., Schvartzman, J. B., Diffley, J.F.X., and Aragón, L. (2011). Positive supercoiling of mitotic DNA drives decatenation by topoisomerase II in eukaryotes. Science. *331*, 1328–1332. https://doi.org/10.1126/science.1201538.
28. Bhat, M.A., Philp, A.V., Glover, D.M., and Bellen, H.J. (1996). Chromatid segregation at anaphase requires the barren product, a novel chromosome-associated protein that interacts with Topoisomerase II. Cell (Cambridge, MA, U. S.) *87*, 1103–1114. https://doi.org/10.1016/s0092-8674(00)81804-8.
29. Earnshaw, W.C., Halligan, B., Cooke, C.A., Heck, M.M., and Liu, L.F. (1985). Topoisomerase II is a structural component of mitotic chromosome scaffolds. J. Cell Biol. *100*, 1706–1715. https://doi.org/10.1083/jcb.100.5.1706.
30. Maeshima, K., and Laemmli, U.K. (2003). A two-step scaffolding model for mitotic chromosome assembly. Dev. Cell *4*, 467–480. https://doi.org/10.1016/s1534-5807(03)00092-3.
31. Ono, T., Losada, A., Hirano, M., Myers, M.P., Neuwald, A.F., and Hirano, T. (2003). Differential contributions of condensin I and condensin II to mitotic chromosome architecture in vertebrate cells. Cell (Cambridge, MA, U. S.) *115*, 109–121. https://doi.org/10.1016/s0092-8674(03)00724-4.
32. Saitoh, N., Goldberg, I.G., Wood, E.R., and Earnshaw, W.C. (1994). ScII: an abundant chromosome scaffold protein is a member of a family of

putative ATPases with an unusual predicted tertiary structure. J. Cell Biol. *127*, 303–318. https://doi.org/10.1083/jcb.127.2.303.

33. Tavormina, P.A., Côme, M.G., Hudson, J.R., Mo, Y.Y., Beck, W.T., and Gorbsky, G.J. (2002). Rapid exchange of mammalian topoisomerase II alpha at kinetochores and chromosome arms in mitosis. J. Cell Biol. *158*, 23–29. https://doi.org/10.1083/jcb.200202053.
34. Losada, A., and Hirano, T. (2001). Intermolecular DNA interactions stimulated by the cohesin complex in vitro: implications for sister chromatid cohesion. Curr. Biol. *11*, 268–272. https://doi.org/10.1016/s0960-9822(01)00066-5.
35. Watson, J.D., and Crick, F.H. (1953). Molecular structure of nucleic acids; a structure for deoxyribose nucleic acid. Nature (London) *171*, 737–738. https://doi.org/10.1038/171737a0.
36. Shure, M., Pulleyblank, D.E., and Vinograd, J. (1977). The problems of eukaryotic and prokaryotic DNA packaging and in vivo conformation posed by superhelix density heterogeneity. Nucleic Acids Res. *4*, 1183–1205. https://doi.org/10.1093/nar/4.5.1183.
37. Arumugam, P., Gruber, S., Tanaka, K., Haering, C.H., Mechtler, K., and Nasmyth, K. (2003). ATP hydrolysis is required for cohesin's association with chromosomes. Curr. Biol. *13*, 1941–1953. https://doi.org/10.1016/j.cub.2003.10.036.
38. Lammens, A., Schele, A., and Hopfner, K.P. (2004). Structural biochemistry of ATP-driven dimerization and DNA-stimulated activation of SMC ATPases. Curr. Biol. *14*, 1778–1782. https://doi.org/10.1016/j.cub.2004.09.044.
39. Janissen, R., Barth, R., Davidson, I.F., Peters, J.M., and Dekker, C. (2024). All eukaryotic SMC proteins induce a twist of -0.6 at each DNA loop extrusion step. Sci. Adv. *10*, eadt1832. https://doi.org/10.1126/sciadv.adt1832.
40. Murayama, Y., and Uhlmann, F. (2015). DNA Entry into and Exit out of the Cohesin Ring by an Interlocking Gate Mechanism. Cell (Cambridge, MA, U. S.) *163*, 1628–1640. https://doi.org/10.1016/j.cell.2015.11.030.
41. Haering, C.H., Farcas, A.M., Arumugam, P., Metson, J., and Nasmyth, K. (2008). The cohesin ring concatenates sister DNA molecules. Nature (London) *454*, 297–301. https://doi.org/10.1038/nature07098.
42. Nagasaka, K., Davidson, I.F., Stocsits, R.R., Tang, W., Wutz, G., Batty, P., Panarotto, M., Litos, G., Schleiffer, A., Gerlich, D.W., and Peters, J.M. (2023). Cohesin mediates DNA loop extrusion and sister chromatid cohesion by distinct mechanisms. Mol. Cell *83*, 3049–3063.e6. https://doi.org/10.1016/j.molcel.2023.07.024.
43. Kueng, S., Hegemann, B., Peters, B.H., Lipp, J.J., Schleiffer, A., Mechtler, K., and Peters, J.M. (2006). Wapl controls the dynamic association of cohesin with chromatin. Cell (Cambridge, MA, U. S.) *127*, 955–967. https://doi.org/10.1016/j.cell.2006.09.040.
44. Haarhuis, J.H.I., van der Weide, R.H., Blomen, V.A., Yáñez-Cuna, J.O., Amendola, M., van Ruiten, M.S., Krijger, P.H.L., Teunissen, H., Medema, R.H., van Steensel, B., et al. (2017). The Cohesin Release Factor WAPL Restricts Chromatin Loop Extension. Cell (Cambridge, MA, U. S.) *169*, 693–707.e14. https://doi.org/10.1016/j.cell.2017.04.013.
45. Tedeschi, A., Wutz, G., Huet, S., Jaritz, M., Wuensche, A., Schirghuber, E., Davidson, I.F., Tang, W., Cisneros, D.A., Bhaskara, V., et al. (2013). Wapl is an essential regulator of chromatin structure and chromosome segregation. Nature (London) *501*, 564–568. https://doi.org/10.1038/nature12471.
46. Neguembor, M.V., Martin, L., Castells-García, Á., Gómez-García, P.A., Vicario, C., Carnevali, D., AlHaj Abed, J., Granados, A., Sebastian-Perez, R., Sottile, F., et al. (2021). Transcription-mediated supercoiling regulates genome folding and loop formation. Mol. Cell *81*, 3065–3081.e3012. https://doi.org/10.1016/j.molcel.2021.06.009.
47. Bird, A. (2025). Cohesin as an essential disruptor of chromosome organization. Mol. Cell *85*, 1054–1057. https://doi.org/10.1016/j.molcel.2025.01.010.
48. Flyamer, I.M., Gassler, J., Imakaev, M., Brandão, H.B., Ulianov, S.V., Abdennur, N., Razin, S.V., Mirny, L.A., and Tachibana-Konwalski, K. (2017). Single-nucleus Hi-C reveals unique chromatin reorganization at oocyte-to-zygote transition. Nature (London) *544*, 110–114. https://doi.org/10.1038/nature21711.
49. Bürmann, F., Funke, L.F.H., Chin, J.W., and Löwe, J. (2021). Cryo-EM structure of MukBEF reveals DNA loop entrapment at chromosomal unloading sites. Mol. Cell *81*, 4891–4906.e4898. https://doi.org/10.1016/j.molcel.2021.10.011.
50. Ryu, J.-K., Rah, S.-H., Janissen, R., Kerssemakers, J.W.J., Bonato, A., Michieletto, D., and Dekker, C. (2022). Condensin extrudes DNA loops in steps up to hundreds of base pairs that are generated by ATP binding events. Nucleic Acids Res. *50*, 820–832. https://doi.org/10.1093/nar/gkab1268.
51. Guérin, T.M., Barrington, C., Pobegalov, G., Molodtsov, M.I., and Uhlmann, F. (2024). An extrinsic motor directs chromatin loop formation by cohesin. EMBO J. *43*, 4173–4196. https://doi.org/10.1038/s44318-024-00202-5.
52. de Wit, E., Vos, E.S.M., Holwerda, S.J.B., Valdes-Quezada, C., Verstegen, M.J.A.M., Teunissen, H., Splinter, E., Wijchers, P.J., Krijger, P.H.L., and de Laat, W. (2015). CTCF Binding Polarity Determines Chromatin Looping. Mol. Cell *60*, 676–684. https://doi.org/10.1016/j.molcel.2015.09.023.
53. Fudenberg, G., Imakaev, M., Lu, C., Goloborodko, A., Abdennur, N., and Mirny, L.A. (2016). Formation of Chromosomal Domains by Loop Extrusion. Cell Rep. *15*, 2038–2049. https://doi.org/10.1016/j.celrep.2016.04.085.
54. Rao, S.S.P., Huntley, M.H., Durand, N.C., Stamenova, E.K., Bochkov, I.D., Robinson, J.T., Sanborn, A.L., Machol, I., Omer, A.D., Lander, E.S., and Aiden, E.L. (2014). A 3D map of the human genome at kilobase resolution reveals principles of chromatin looping. Cell (Cambridge, MA, U. S.) *159*, 1665–1680. https://doi.org/10.1016/j.cell.2014.11.021.
55. Sanborn, A.L., Rao, S.S.P., Huang, S.C., Durand, N.C., Huntley, M.H., Jewett, A.I., Bochkov, I.D., Chinnappan, D., Cutkosky, A., Li, J., et al. (2015). Chromatin extrusion explains key features of loop and domain formation in wild-type and engineered genomes. Proc. Natl. Acad. Sci. USA *112*, E6456–E6465. https://doi.org/10.1073/pnas.1518552112.
56. Vietri Rudan, M., Barrington, C., Henderson, S., Ernst, C., Odom, D.T., Tanay, A., and Hadjur, S. (2015). Comparative Hi-C reveals that CTCF underlies evolution of chromosomal domain architecture. Cell Rep. *10*, 1297–1309. https://doi.org/10.1016/j.celrep.2015.02.004.
57. Ganji, M., Shaltiel, I.A., Bisht, S., Kim, E., Kalichava, A., Haering, C.H., and Dekker, C. (2018). Real-time imaging of DNA loop extrusion by condensin. Science. *360*, 102–105. https://doi.org/10.1126/science.aar7831.
58. Banigan, E.J., Tang, W., van den Berg, A.A., Stocsits, R.R., Wutz, G., Brandão, H.B., Busslinger, G.A., Peters, J.M., and Mirny, L.A. (2023). Transcription shapes 3D chromatin organization by interacting with loop extrusion. Proc. Natl. Acad. Sci. USA *120*, e2210480120. https://doi.org/10.1073/pnas.2210480120.
59. Morao, A.K., Kim, J., Obaji, D., Sun, S., and Ercan, S. (2022). Topoisomerases I and II facilitate condensin DC translocation to organize and repress X chromosomes in C. elegans. Mol. Cell *82*, 4202–4217.e5. https://doi.org/10.1016/j.molcel.2022.10.002.
60. Nishiyama, T., Ladurner, R., Schmitz, J., Kreidl, E., Schleiffer, A., Bhaskara, V., Bando, M., Shirahige, K., Hyman, A.A., Mechtler, K., and Peters, J.M. (2010). Sororin mediates sister chromatid cohesion by antagonizing Wapl. Cell (Cambridge, MA, U. S.) *143*, 737–749. https://doi.org/10.1016/j.cell.2010.10.031.
61. Weissmann, F., Petzold, G., VanderLinden, R., Huis In 't Veld, P.J., Brown, N.G., Lampert, F., Westermann, S., Stark, H., Schulman, B.A., and Peters, J.M. (2016). biGBac enables rapid gene assembly for the expression of large multisubunit protein complexes. Proc. Natl. Acad. Sci. USA *113*, E2564–E2569. https://doi.org/10.1073/pnas.1604935113.
62. Fellmann, C., Hoffmann, T., Sridhar, V., Hopfgartner, B., Muhar, M., Roth, M., Lai, D.Y., Barbosa, I.A.M., Kwon, J.S., Guan, Y., et al. (2013). An Optimized microRNA Backbone for Effective Single-Copy RNAi. Cell Rep. *5*, 1704–1713. https://doi.org/10.1016/j.celrep.2013.11.020.

63. Short, J.M., Fernandez, J.M., Sorge, J.A., and Huse, W.D. (1988). λ ZAP: a bacteriophage λ expression vector with in vivo excision properties. Nucleic Acids Res. *16*, 7583–7600. https://doi.org/10.1093/nar/16.15.7583.
64. Yesbolatova, A., Saito, Y., Kitamoto, N., Makino-Itou, H., Ajima, R., Nakano, R., Nakaoka, H., Fukui, K., Gamo, K., Tominari, Y., et al. (2020). The auxin-inducible degron 2 technology provides sharp degradation control in yeast, mammalian cells, and mice. Nat. Commun. *11*, 5701. https://doi.org/10.1038/s41467-020-19532-z.
65. Gibson, D.G., Young, L., Chuang, R.Y., Venter, J.C., Hutchison, C.A., 3rd, and Smith, H.O. (2009). Enzymatic assembly of DNA molecules up to several hundred kilobases. Nat. Methods *6*, 343–345. https://doi.org/10.1038/nmeth.1318.
66. Weissmann, F., and Peters, J.M. (2018). Expressing Multi-subunit Complexes Using biGBac. Methods Mol. Biol. *1764*, 329–343. https://doi.org/10.1007/978-1-4939-7759-8_21.
67. Hauf, S., Waizenegger, I.C., and Peters, J.-M. (2001). Cohesin Cleavage by Separase Required for Anaphase and Cytokinesis in Human Cells. Science. *293*, 1320–1323. https://doi.org/10.1126/science.1061376.
68. Charvin, G., Bensimon, D., and Croquette, V. (2003). Single-molecule study of DNA unlinking by eukaryotic and prokaryotic type-II topoisomerases. Proc. Natl. Acad. Sci. USA *100*, 9820–9825. https://doi.org/10.1073/pnas.1631550100.
69. Crisona, N.J., Strick, T.R., Bensimon, D., Croquette, V., and Cozzarelli, N.R. (2000). Preferential relaxation of positively supercoiled DNA by E. coli topoisomerase IV in single-molecule and ensemble measurements. Genes Dev. *14*, 2881–2892. https://doi.org/10.1101/gad.838900.
70. Stone, M.D., Bryant, Z., Crisona, N.J., Smith, S.B., Vologodskii, A., Bustamante, C., and Cozzarelli, N.R. (2003). Chirality sensing by Escherichia coli topoisomerase IV and the mechanism of type II topoisomerases. Proc. Natl. Acad. Sci. USA *100*, 8654–8659. https://doi.org/10.1073/pnas.1133178100.
71. Gellert, M., Mizuuchi, K., O'Dea, M.H., and Nash, H.A. (1976). DNA gyrase: an enzyme that introduces superhelical turns into DNA. Proc. Natl. Acad. Sci. USA *73*, 3872–3876. https://doi.org/10.1073/pnas.73.11.3872.
72. Wang, J.C. (1971). Interaction between DNA and an Escherichia coli protein omega. J. Mol. Biol. *55*, 523–533. https://doi.org/10.1016/0022-2836(71)90334-2.
73. Uchihashi, T., Kodera, N., and Ando, T. (2012). Guide to video recording of structure dynamics and dynamic processes of proteins by high-speed atomic force microscopy. Nat. Protoc. *7*, 1193–1206. https://doi.org/10.1038/nprot.2012.047.
74. Busslinger, G.A., Stocsits, R.R., van der Lelij, P., Axelsson, E., Tedeschi, A., Galjart, N., and Peters, J.M. (2017). Cohesin is positioned in mammalian genomes by transcription, CTCF and Wapl. Nature (London) *544*, 503–507. https://doi.org/10.1038/nature22063.
75. Ngo, K.X., Kodera, N., Katayama, E., Ando, T., and Uyeda, T.Q.P. (2015). Cofilin-induced unidirectional cooperative conformational changes in actin filaments revealed by high-speed atomic force microscopy. eLife *4*, e04806. https://doi.org/10.7554/eLife.04806.
76. Loeff, L., Kerssemakers, J.W.J., Joo, C., and Dekker, C. (2021). AutoStepfinder: A fast and automated step detection method for single-molecule analysis. Patterns *2*, 100256. https://doi.org/10.1016/j.patter.2021.100256.
77. Delft High Performance Computing Centre (DHPC), DelftBlue Supercomputer (Phase 2), https://www.tudelft.nl/dhpc/ark:/44463/DelftBluePhase2. (2024).
78. Kim, E., Kerssemakers, J., Shaltiel, I.A., Haering, C.H., and Dekker, C. (2020). DNA-loop extruding condensin complexes can traverse one another. Nature (London) *579*, 438–442. https://doi.org/10.1038/s41586-020-2067-5.
79. Lipfert, J., Kerssemakers, J.W.J., Jager, T., and Dekker, N.H. (2010). Magnetic torque tweezers: measuring torsional stiffness in DNA and RecA-DNA filaments. Nat. Methods *7*, 977–980. https://doi.org/10.1038/nmeth.1520.
80. Xu, W., Dunlap, D., and Finzi, L. (2021). Energetics of twisted DNA topologies. Biophys. J. *120*, 3242–3252. https://doi.org/10.1016/j.bpj.2021.05.002.
81. Takaki, R., Dey, A., Shi, G., and Thirumalai, D. (2021). Theory and simulations of condensin mediated loop extrusion in DNA. Nat. Commun. *12*, 5865. https://doi.org/10.1038/s41467-021-26167-1.
82. Seol, Y., Zhang, H., Pommier, Y., and Neuman, K.C. (2012). A kinetic clutch governs religation by type IB topoisomerases and determines camptothecin sensitivity. Proc. Natl. Acad. Sci. USA *109*, 16125–16130. https://doi.org/10.1073/pnas.1206480109.
83. Pommier, Y., Nussenzweig, A., Takeda, S., and Austin, C. (2022). Human topoisomerases and their roles in genome stability and organization. Nat. Rev. Mol. Cell Biol. *23*, 407–427. https://doi.org/10.1038/s41580-022-00452-3.
84. Marko, J.F., and Neukirch, S. (2012). Competition between curls and plectonemes near the buckling transition of stretched supercoiled DNA. Phys. Rev. E - Stat. Nonlinear Soft Matter Phys. *85*, 011908. https://doi.org/10.1103/PhysRevE.85.011908.
85. Virtanen, P., Gommers, R., Oliphant, T.E., Haberland, M., Reddy, T., Cournapeau, D., Burovski, E., Peterson, P., Weckesser, W., Bright, J., et al. (2020). SciPy 1.0: fundamental algorithms for scientific computing in Python. Nat. Methods *17*, 261–272. https://doi.org/10.1038/s41592-019-0686-2.
86. Wingett, S., Ewels, P., Furlan-Magaril, M., Nagano, T., Schoenfelder, S., Fraser, P., and Andrews, S. (2015). HiCUP: pipeline for mapping and processing Hi-C data. F1000Res. *4*, 1310. https://doi.org/10.12688/f1000research.7334.1.
87. Durand, N.C., Shamim, M.S., Machol, I., Rao, S.S.P., Huntley, M.H., Lander, E.S., and Aiden, E.L. (2016). Juicer Provides a One-Click System for Analyzing Loop-Resolution Hi-C Experiments. Cell Syst. *3*, 95–98. https://doi.org/10.1016/j.cels.2016.07.002.
88. Heinz, S., Benner, C., Spann, N., Bertolino, E., Lin, Y.C., Laslo, P., Cheng, J.X., Murre, C., Singh, H., and Glass, C.K. (2010). Simple Combinations of Lineage-Determining Transcription Factors Prime cis-Regulatory Elements Required for Macrophage and B Cell Identities. Mol. Cell *38*, 576–589. https://doi.org/10.1016/j.molcel.2010.05.004.
89. Sato, Y., Nakajima, S., Shiraga, N., Atsumi, H., Yoshida, S., Koller, T., Gerig, G., and Kikinis, R. (1998). Three-dimensional multi-scale line filter for segmentation and visualization of curvilinear structures in medical images. Med. Image Anal. *2*, 143–168. https://doi.org/10.1016/S1361-8415(98)80009-1.
90. Spencer, S.L., Cappell, S.D., Tsai, F.-C., Overton, K.W., Wang, C.L., and Meyer, T. (2013). The Proliferation-Quiescence Decision Is Controlled by a Bifurcation in CDK2 Activity at Mitotic Exit. Cell (Cambridge, MA, U. S.) *155*, 369–383. https://doi.org/10.1016/j.cell.2013.08.062.

STAR★METHODS

KEY RESOURCES TABLE

REAGENT or RESOURCE	SOURCE	IDENTIFIER
Antibodies		
SMC1 (western blotting)	In-house	A1027
SMC3 (western blotting)	Thermo Fisher Scientific	RRID: AB_67579
Acetyl-SMC3 (western blotting)	Nishiyama et al.[60]	N/A
HA	BioLegend	MMS-101P
WAPL (western blotting)	In-house	A1017
Tubulin (western blotting)	Sigma	RRID: AB_477579
Histone H3 (western blotting)	Cell Signaling Technology	RRID: AB_331563
TOP1 (western blotting)	Abcam	RRID:AB_10861978
TOP2A (western blotting)	Santa Cruz	RRID: AB_10611755
TOP2B (western blotting)	Novus Biologicals	RRID: AB_792364
SMC3 (immunofluorescence microscopy)	In house	A941
Digoxigenin antibodies	Roche	RRID: AB_514496
Bacterial and virus strains		
E. coli DH5alpha	In-house	N/A
DH10MultiBAC DH10EmBacY	In-house	N/A
Chemicals, peptides, and recombinant proteins		
Fugene 6	Promega	E2691
Ni-NTA agarose	Qiagen	30230
Flag M2 agarose beads	Sigma	A2220-25ML
Toyopearl AF-Chelate-650M	Tosoh	0014475
BSA	Thermo Fisher Scientific	AM2616
ATP	Jena Biosciences	NU-1049
Pluronic F-127	Sigma	P2443
Fetal calf serum	Gibco	A5256801
L-glutamine	Gibco	25030–024
Penicillin/Streptomycin	Sigma	P0781
Poloxamer 188	Gibco	24040–032
Bismaleimidoethane (BMOE)	ThermoFisher Scientific	22323
Chloroquine diphosphate	Sigma	C6628
cOmplete EDTA-free protease inhibitor	Roche	11873580001
Benzonase	In-house	N/A
DNase	In-house	N/A
Proteinase K	Sigma	P6556
Phenol:chloroform:isoamyl alcohol	Sigma	P2069
Chloroform	Sigma	P32211
Sybr Gold	ThermoFisher Scientific	S11494
Ampure XP Reagent	Beckmann	A63881
E. coli DNA gyrase	Inspiralis	G1001
E. coli Topo IV	Inspiralis	TD002
E. coli TopA	New England Biolabs	M0301L
Glass rods	Hilgenberg GmbH	7001854
Mica sheets	RIBM	
Cantilevers	Nanoworld	USC-F1.2-k0.15-10

(*Continued on next page*)

Continued

REAGENT or RESOURCE	SOURCE	IDENTIFIER
Streptavidin-coated Superparamagnetic beads MyOne	Thermo Fischer	65601
3.4 kb torsionally constrained dsDNA	Janissen et al.[39]	N/A
Polystyrene beads 1.5 µm	Polysciences Europe	17133
dTAG7	TOCRIS Bioscience	6912
Indole-3-Acdtic Acid (Auxin)	GoldBio	1-110-25
5-Ph-IAA (Auxin 2)	Bio Academia	30–003
Doxycycline hydrochloride	Sigma	D-9891
Blasticidin S	Gibco	R210-01
DMEM phenol red free	Gibco	041-96205M
DAPI	Sigma	D9542
Hoechst 33342	Invitrogen	H3570
HaloTag TMR ligand	Promega	G8251
Puromycin-dihydrochlorid	Sigma-Aldrich	P9620
Geneticin G418	Gibco	11811–031
HaloTag Ligand Building Blocks Succinimidyl Ester 02 Ligand	Promega	P1691
Deposited data		
Hi-C	This paper	GEO: GSE292596
Simulation code	This paper	4TU.ResearchData: https://data.4tu.nl/private_datasets/2V3F14Y-Y2A3XQEf9EN6Pj7o6pXaTL2m62-LCX5Ng9w
Experimental models: Cell lines		
Sf9 insect cells	Thermo Fisher Scientific	B82501
HeLa SMC1-AID-mKate2/SCC1-Halo-P2A-TIR1/Blast-P2A-HA-FKBP12^{F36V}-WAPL	Nagasaka et al.[42]	N/A
HeLa SMC1-AID-mKate2/SCC1-Halo-P2A-TIR1/Blast-P2A-HA-FKBP12^{F36V}-WAPL SMC1-WT	This paper	N/A
HeLa SMC1-AID-mKate2/SCC1-Halo-P2A-TIR1/Blast-P2A-HA-FKBP12^{F36V}-WAPL SMC1-4E	This paper	N/A
HeLa SMC1-AID-mKate2/SCC1-Halo-P2A-TIR1/Blast-P2A-HA-FKBP12^{F36V}-WAPL/GFP-P2A-HA-FKBP12^{F36V}-CTCF	This paper	N/A
HeLa SMC1-AID-mKate2/SCC1-Halo-P2A-TIR1/Blast-P2A-HA-FKBP12^{F36V}-WAPL/GFP-P2A-HA-FKBP12^{F36V}-CTCF SMC1-WT	This paper	N/A
HeLa SMC1-AID-mKate2/SCC1-Halo-P2A-TIR1/Blast-P2A-HA-FKBP12^{F36V}-WAPL/GFP-P2A-HA-FKBP12^{F36V}-CTCF SMC1-4E	This paper	N/A
HeLa HA- FKBP12^{F36V}-WAPL	Banigan et al.[58]	N/A
HeLa TOP1-AID2-mClover/HA-FKBP12^{F36V}-WAPL	This paper	N/A
HeLa TOP2A-AID2-mClover/mKate2-AID2-TOP2B/HA- FKBP12^{F36V}-WAPL	This paper	N/A
LentiX cells	Takara	632180

(*Continued on next page*)

Continued

REAGENT or RESOURCE	SOURCE	IDENTIFIER
Oligonucleotides		
See Table S2		
Recombinant DNA		
pH6HTN	Promega	G7971
pLib	Weissmann et al.[61]	RRID:Addgene_80610
pBig1a	Weissmann et al.[61]	RRID:Addgene_80611
pBig1b	Weissmann et al.[61]	RRID:Addgene_80612
pBig2ab	Weissmann et al.[61]	RRID:Addgene_80616
LT3GEPIR	Fellmann et al.[62]	RRID:Addgene_111177
pBSKII	Short et al.[63]	GenBank: X52327.1
pRRL-PGK	Wutz et al.[4]	N/A
Software and algorithms		
Fiji	NIH	Version 2.16.0
Prism	Graphpad	Version 10
LabView 20	National Instruments	Version 2011
IgorPro	Wavemetrics	Version 6.37
Python	Python.org	Version 3.10
Zen	Zeiss	Black and blue editions
R Studio	Prairie Trillium	2022.02.3

EXPERIMENTAL MODEL AND STUDY PARTICIPANT DETAILS

Cloning procedures were carried out in *Escherichia coli* DH5α. Bacmids were generated in *E. coli* DH10EmBacY as described in the “protein expression and purification” section. *E. coli* strains were grown at 37°C in LB (prepared in-house).

Spodoptera frugiperda Sf9 cells derived from pupal ovarian tissue of the female fall armyworm (Thermo Fisher Scientific; B82501) were cultured at 100 rpm and 27°C in Grace medium (prepared in-house) supplemented with 10% fetal calf serum (Gibco; A5256801), 2 mM L-glutamine (Gibco; 25030-024), 1x Penicillin-Streptomycin (Sigma-Aldrich; P0781) and 0.1% Poloxamer 188 (Gibco; 24040-032). Sf9 cultures were infected with baculoviruses for recombinant protein expression as described in the “protein expression and purification” section.

The HeLa Kyoto (female) cell lines used in this study are listed in the Key Resources Table. All cell lines were free from detectable mycoplasma contamination and have been authenticated by STR fingerprinting (Vienna Biocenter Core Facilities). HeLa Kyoto cells were cultured at 37°C, 5% CO$_2$ in DMEM (prepared in-house) supplemented with 10% fetal calf serum (Gibco; A5256801), 2 mM L-glutamine (Gibco; 25030-024) 1x Penicillin-Streptomycin (Sigma-Aldrich; P0781) as described.[42] The SMC1-AID-mKate2/SCC1-Halo-P2A-TIR1/Blasticidin-P2A-HA-FKBP12^{F36V}-WAPL/GFP-P2A-HA-FKBP12^{F36V}-CTCF HeLa Kyoto cell line was created based on the SMC1-AID-mKate2/SCC1-Halo-P2A-TIR1/Blast-P2A-HA-FKBP12^{F36V}-WAPL cell line described previously.[42] The gRNA sequences that were used to target CTCF are as follows: TTTCCCCTGCCTTTATTAA and GATGCAGTCGAAGCCATTG. GFP positive clones were isolated by FACS sorting. Homozygous integration was verified by western blot and PCR of genomic DNA using the following primers: CTCCCTCCAATCAGTCTTCCC and AGAACGGTACCCACATAACGA.

SMC1-AID-mKate2/SCC1-Halo-P2A-TIR1/Blasticidin-P2A-HA-FKBP12^{F36V}-WAPL cells[42] and SMC1-AID-mKate2/SCC1-Halo-P2A-TIR1/Blasticidin-P2A-HA-FKBP12^{F36V}-WAPL/GFP-P2A-HA-FKBP12^{F36V}-CTCF cells (described above) were infected with lentiviruses as described[42] to generate wildtype SMC1 or SMC1^{4E}-expressing cells.

The TOP1-AID2-mClover/HA- FKBP12^{F36V}-WAPL and TOP2A-AID2-mClover/mKate2-AID2-TOP2B/HA- FKBP12^{F36V}-WAPL HeLa Kyoto cell lines were created based on the HA- FKBP12^{F36V}-WAPL cell line described previously[58] using auxin-inducible degron 2 technology.[64] The gRNA sequences that were used are as follows: TOP1: CACCGGAGGCAGAGTTCTGTGAAG; TOP2A: CACCGGTAACTTTAAAACCAGTCT; TOP2B: CACCGCAGCCACCCGACTTGGCCA. Clones were selected after verification of homozygous integration by PCR of genomic DNA using the following primers: TOP1: GTTACTCTGGTTGCTGAACCTTG and ACTGGCTCAGCTCTCCCTTAT; TOP2A: GCCAAAACCAAGAATCGCCG and TGGATCAAATGTTGTCCCCGA; TOP2B: AAACAG CACGCTTGGAGGAT and TGCGATGCTGACGTAGACAA.

The sample sizes analyzed in this study are as follows: Figures 2C–2E: N = 102, 104, 108, 108 plasmids analyzed per no cohesin, wild type cohesin, cohesin-SMC14E and cohesin$^{EQ/EQ}$ condition, respectively. Figure 3B: N = 54 DNAs. Figure 3D: N = 24 DNAs. Figure 4F: N = 20, 21, 19, 14, 20, 14, 22 cells per condition, ordered left-to-right as displayed in Figure 4F. Figure 4G: N = 12

(WT + aux), 12 (WT+dTAG+aux), 13 (SMC1 4E + aux), 12 (SMC1 4E+dTAG+aux) cells. Figure 6C: *N* = 49, 55, 46, 58, 50, 54, 43, 40 cells per condition, ordered left-to-right as displayed in Figure 6C.

METHOD DETAILS

Cloning and mutagenesis

A list of all constructs used in this manuscript is shown in Table S3. Site-directed mutagenesis using Phusion Hot Start Flex DNA Polymerase (NEB) was used to introduce the individual "1E" mutations (K52E, R57E, K59E, K62E) into pLib SMC1, S1129R into pLib SMC1, S1116R into pLib SMC3-FLAG, and E1157Q and S1129R into pLib SMC1^{4E}. All other constructs produced in this study were generated using Gibson Assembly.[65]

SMC1 and SMC3 expression cassettes from pLib constructs were typically combined into bigBAC pBig1a polycistronic expression vectors.[61] SCC1 and STAG1 expression cassettes were typically combined into pBig1b vectors.[61]

Protein expression

pLib, pBig1a, pBig1b and pBig2ab vectors were transformed into DH10EmBacY *E. coli* cells and bacmid DNA was isolated as described.[66] 1x10^6 Sf9 cells were seeded on a 6 well plate in 3 mL Sf-900 SFM media (ThermoFisher Scientific; 12658027), transfected with bacmid DNA using Fugene 6 (Promega) and incubated for 96 h at 27°C. The baculovirus-containing cell supernatant (V0) was then collected and used to infect 50 mL Sf9 cells at a density of 1 x10^6 cells/ml in Grace medium (prepared in-house) supplemented with 10% fetal calf serum (Gibco; A5256801), 2 mM L-glutamine (Gibco; 25030-024), 1x Penicillin-Streptomycin (Sigma-Aldrich; P0781) and 0.1% Poloxamer 188 (Gibco; 24040-032). Cells were grown at 100 rpm and 27°C, centrifuged 72 h after infection and 9 mL cell supernatant (V1) was then used to infect 750 mL Sf9 cells at a density of 1.2 x10^6 cells/ml in Grace medium supplemented as above. Between one and four 750 mL cultures were infected per construct, depending on the predicted yield of recombinant protein. Cells were centrifuged around 54 h after infection, washed in PBS, frozen in liquid nitrogen and stored at −80°C.

For the expression of wild type tetrameric cohesin, Sf9 insect cells were either co-infected with baculoviruses generated from pBig1a SMC1_SMC3-FLAG (Table S3; construct #1) and pBig1b SCC1$^{R172A/D279A/R450A}$-HALO_10xHIS-STAG1 vectors (Table S3; construct #2; the R172A/D279A/R450A mutations in SCC1 prevent separase and caspase cleavage[17,67]) or were infected with a baculovirus generated from a pBig2ab SMC1_SMC3-FLAG_ SCC1$^{R172A/D279A/R450A}$-HALO_10xHIS-STAG1 vector (Table S3; construct #3). All mutant forms of tetrameric cohesin were generated by co-infection of the corresponding mutated SMC1/SMC3 pBig1a baculovirus and a pBig1b SCC1$^{R172A/D279A/R450A}$-HALO_10xHIS-STAG1 (Table S3; construct #2) baculovirus. For the expression of wild type trimeric cohesin, Sf9 insect cells were infected with a baculovirus generated from a pBig2ab SMC1_SMC3-FLAG_ HIS-SCC1 (TEV)-HALO vector (Table S3; construct #22). For the expression of single-chain trimeric cohesin, Sf9 insect cells were infected with a baculovirus generated from a pLib single-chain cohesin vector (Table S3; construct #23).

Cohesin and NIPBL-MAU2 purification

Wild type and mutant forms of recombinant cohesin (see above for expression strategy), as well as NIPBL-MAU2 (Table S3; construct #4) were purified from around 20 mL Sf9 cell pellets essentially as described.[10] All steps were performed at 4°C unless indicated otherwise. Cohesin or NIPBL-MAU2 cell pellets were lysed by Dounce homogenization in buffer 1 (25 mM NaH_2PO_4/Na_2HPO_4 [pH 7.5], 500 mM NaCl, 5% glycerol) supplemented with 10 mM imidazole [pH 7.5], 0.05% Tween 20, 1 mM PMSF, 3 mM betamercaptoethanol, 10 μg/mL aprotinin, 10 μg/mL leupeptin, 10 μg/mL chymostatin, 10 μg/mL pepstatin A, 2 mM benzamidine (Sigma), cOmplete EDTA-free protease inhibitor cocktail (Merck; 11873580001), DNase I (800 units) and benzonase (prepared in-house). After centrifugation (48000 g, 45 min), the soluble fraction was combined with 5 mL of Toyopearl AF-chelate-650M resin (Tosoh Bioscience) pre-charged with Ni^{2+} ions and incubated for 3 h. Beads were washed with 3 x 10 bead volumes of buffer 1 supplemented with 15 mM imidazole [pH 7.5], 0.01% Tween 20. Bound protein was eluted with 25 mL buffer 2 (25 mM Na_2HPO_4/NaH_2PO_4 [pH 7.5], 150 mM NaCl, 5% glycerol, 300 mM imidazole [pH 7.5], 0.01% Tween 20). The eluate was then combined with 5 mL of FLAG-M2 agarose resin (Sigma; A2220) and incubated for three hours. Beads were washed with 3 x 10 bead volumes of buffer 3 (25 mM Na_2HPO_4/NaH_2PO_4 [pH 7.5], 150 mM NaCl, 5% glycerol, 50 mM imidazole [pH 7.5]) and eluted with 25 mL buffer 3 supplemented with 0.5 mg/mL 3xFLAG peptide. Eluates were concentrated to ~0.5 mL using Vivaspin 20 100 kDa MWCO ultrafiltration units (Sartorius; VS2042), frozen in liquid nitrogen and stored at −80°C.

Single-chain trimeric cohesin purification

Single-chain trimeric cohesin (Table S3; construct #23) was purified from around 40 mL Sf9 cell pellets essentially as described.[10] All steps were performed at 4°C unless indicated otherwise. Around 40 mL cell pellet was lysed by Dounce homogenization in 5 volumes of single-chain buffer (50 mM NaH_2PO_4/Na_2HPO_4 [pH 7.5], 500 mM NaCl, 5% glycerol) supplemented with 0.05% Tween 20, 1 mM PMSF, 10 μg/mL aprotinin, 10 μg/mL leupeptin, 10 μg/mL chymostatin, 10 μg/mL pepstatin A, 2 mM benzamidine (Sigma) and cOmplete EDTA-free protease inhibitor cocktail. Lysates were cleared by centrifugation (40000 g, 45 min) and supernatants were applied to 5 mL FLAG M2 agarose for 3 h. Beads were washed once with 50 mL single-chain buffer supplemented with 0.05% Tween 20, once with 50 mL single-chain buffer and once with 50 mL low salt buffer (NaH_2PO_4/Na_2HPO_4 [pH 7.5], 100 mM NaCl, 5% glycerol) followed by elution into 5 volumes of low salt buffer supplemented with 0.25 mg/mL 3xFLAG peptide. The eluate was loaded at

1 mL/min on a 1 mL POROS HS column (ThermoFisher Scientific) in low salt buffer supplemented with 0.5mM TCEP. The column was washed until baseline absorption and single-chain cohesin was eluted with a linear gradient (40% B in 60 min at 1 mL/min) of high salt buffer (NaH_2PO_4/Na_2HPO_4 [pH 7.5], 1.2 M NaCl, 5% glycerol, 0.5 mM TCEP). Fractions containing cohesin were pooled, concentrated, frozen in liquid nitrogen and stored at −80°C.

STAG1 purification

STAG1 (Table S3; construct #24) was purified from around 40 mL Sf9 cell pellets essentially as described.[10] All steps were performed at 4°C unless indicated otherwise. Around 40 mL cell pellet was lysed by Dounce homogenization in STAG1 purification buffer 1 (50 mM NaH_2PO_4/Na_2HPO_4 [pH 7.6], 500 mM NaCl, 5% glycerol) supplemented with 15 mM imidazole [pH 7.5], 0.05% Tween 20, 1 mM PMSF, 3 mM betamercaptoethanol, 10 μg/mL aprotinin, 10 μg/mL leupeptin, 10 μg/mL chymostatin, 10 μg/mL pepstatin A, 2 mM benzamidine (Sigma) and cOmplete EDTA-free protease inhibitor cocktail. After centrifugation (48000 g, 45 min), the soluble fraction was combined with 2 mL of NiNTA agarose (Qiagen; 30230) and incubated for 2 h. Beads were washed with 1 x 25 bead volumes of STAG1 purification buffer supplemented with 3 mM betamercaptoethanol, 2 mM benzamidine, 20 mM imidazole [pH 7.5] and 0.05% Tween 20 and then 2 x 25 bead volumes of STAG1 purification buffer supplemented with 20 mM imidazole [pH 7.5] and 0.05% Tween 20. Bound protein was eluted with 15 mL STAG1 elution buffer (50 mM Na_2HPO_4/NaH_2PO_4 [pH 7.6], 150 mM NaCl, 5% glycerol, 300 mM imidazole [pH 7.5]). Eluted protein was supplemented with 1 mM DTT and concentrated to around 0.5 mL using Vivaspin 6 50 kDa MWCO ultrafiltration units (Sartorius; VS0631), filtered and applied to a Superdex 200 10/300 GL column at 0.4 mL/min equilibrated in size exclusion buffer (50 mM Na_2HPO_4/NaH_2PO_4 [pH 7.5], 150 mM NaCl, 5% glycerol, 1 mM DTT). Fractions containing STAG1 were pooled, concentrated, frozen in liquid nitrogen and stored at −80°C.

PDS5A purification

All steps were performed at 4°C unless indicated otherwise. Around 20 mL Sf9 cell pellet (Table S3; construct #5) was thawed and lysed by Dounce homogenization in PDS5 purification buffer (25 mM Na_2HPO_4/NaH_2PO_4 [pH 7.5], 500 mM NaCl, 5% glycerol) supplemented with 10 mM imidazole [pH 7.5], 0.05% Tween 20, 1 mM PMSF, 3 mM betamercaptoethanol, 10 μg/mL aprotinin, 10 μg/mL leupeptin, 10 μg/mL chymostatin, 10 μg/mL pepstatin A, 2 mM benzamidine and cOmplete EDTA-free protease inhibitor cocktail (Merck; 11873580001). After centrifugation (47000 g, 45 min), the soluble fraction was combined with 1 mL of NiNTA agarose (Qiagen; 30230) and incubated for 90 min. Beads were washed with 3 x 20 bead volumes of PDS5 purification buffer supplemented with 30 mM imidazole [pH 7.5] and 3 mM betamercaptoethanol. Bound protein was eluted with 6 mL PDS5 elution buffer (25 mM Na_2HPO_4/NaH_2PO_4 [pH 7.5], 150 mM NaCl, 5% glycerol, 300 mM imidazole [pH 7.5], 1 mM DTT). Eluted protein was concentrated to around 0.5 mL using Vivaspin 6 50 kDa MWCO ultrafiltration units (Sartorius; VS0631), filtered and applied to a Superdex 200 10/300 GL column at 0.4 mL/min equilibrated in size exclusion buffer (25 mM Na_2HPO_4/NaH_2PO_4 [pH 7.5], 150 mM NaCl, 5% glycerol, 1 mM DTT). Fractions containing PDS5A were pooled, concentrated, frozen in liquid nitrogen and stored at −80°C.

Human topoisomerase I purification

All steps were performed at 4°C unless indicated otherwise. Around 20 mL Sf9 cell pellet (Table S3; construct #18) was thawed and lysed by Dounce homogenization in TopoI purification buffer 1 (25 mM Na_2HPO_4/NaH_2PO_4 [pH 7.5], 500 mM NaCl, 5% glycerol) supplemented with 10 mM imidazole [pH 7.5], 0.05% Tween 20, 1 mM PMSF, 3 mM betamercaptoethanol, 10 μg/mL aprotinin, 10 μg/mL leupeptin, 10 μg/mL chymostatin, 10 μg/mL pepstatin A, 2 mM benzamidine and cOmplete EDTA-free protease inhibitor cocktail (Merck; 11873580001). After centrifugation (47000 g, 45 min), the soluble fraction was combined with 4 mL of Toyopearl AF-chelate-650M resin (Tosoh Bioscience) pre-charged with Ni^{2+} ions and incubated for 2 h. Beads were washed with 3 x 10 bead volumes of TopoI purification buffer 1 supplemented with 25 mM imidazole [pH 7.5]. Bound protein was eluted with 25 mL TopoI purification buffer 2 (25 mM Na_2HPO_4/NaH_2PO_4 [pH 7.5], 150 mM NaCl, 5% glycerol, 300 mM imidazole [pH 7.5]). The eluate was then combined with 5 mL of FLAG-M2 agarose resin (Sigma; A2220) and incubated for three hours. Beads were washed with 3 x 10 bead volumes of TopoI purification buffer 3 (25 mM Na_2HPO_4/NaH_2PO_4 pH 7.5, 150 mM NaCl, 5% glycerol, 50 mM imidazole pH 7.5). Bound protein was eluted with 15 mL TopoI purification buffer 3 supplemented with 0.5 mg/mL 3xFlag peptide. Eluates were concentrated to ∼0.75 mL using Vivaspin 20 100 kDa MWCO ultrafiltration units (Sartorius; VS2042), frozen in liquid nitrogen and stored at −80°C.

Human topoisomerase I plasmid supercoiling assay

Negatively supercoiled plasmid DNA (pH6HTN (Promega), 4 kb) was relaxed by incubating it together with human topoisomerase I for 45 min at 37°C. This mixture was then supplemented with recombinant human cohesin and NIPBL-MAU2 as indicated and incubated for a further 90 min (final reaction conditions: 20 mM Na_2HPO_4/NaH_2PO_4 [pH 7.5], 5 mM Tris [pH 7.5], 25 mM NaCl, 2.5 mM $MgCl_2$, 1 mM DTT, 0.1 mg/mL BSA (Thermo Fisher Scientific; AM2616), 2 mM ATP (Jena Biosciences; NU-1049), 0.4 nM pH6HTN, 3 nM human topoisomerase I, 0–32 nM cohesin (corresponding to a cohesin/plasmid molar ratio of up to 80:1) and 0–64 nM NIPBL-MAU2 (i.e., a 2-fold molar excess relative to cohesin) in a 100 μL reaction). Reactions were stopped by addition of sodium dodecyl sulfate (SDS; 0.33% final), EDTA (6.7 mM final) and Proteinase K (0.1 mg/mL final; Sigma-Aldrich; P6556) and incubated for 40 min at 50°C. DNA was extracted using phenol:chloroform:isoamyl alcohol (Sigma-Aldrich; P2069) and then chloroform (Sigma-Aldrich; P32211) in 5PRIME Phase Lock Gel Light tubes (Quantabio; 2302820). Purified DNA was supplemented with glycerol to 10% final concentration and trace amounts of Orange G (Sigma-Aldrich; P2069). Half of the reaction volume were electrophoresed in a

0.7% agarose gel in 1x TBE buffer supplemented with 0.4 μg/mL chloroquine (Sigma-Aldrich; C6628) for 17 h at 32 V. Gels were stained with Sybr Gold (Thermo Fisher Scientific; S11494) and visualized using a ChemiDoc MP imager (Bio-Rad). All gel images are representative of at least two independent experiments.

Single-chain cohesin plasmid supercoiling assay

Single-chain cohesin was incubated on ice in a 12.6 μL reaction (final reaction conditions: 245 nM single-chain cohesin, 25 mM Na_2HPO_4/NaH_2PO_4 [pH 7.5], 150 mM NaCl, 50 mM imidazole pH 7.5, 5% glycerol, 238 μM bismaleimidoethane (BMOE; Thermo Fisher Scientific; 22323). After 10 min, the crosslinking reaction was quenched by addition of DTT to 10 mM. Non-crosslinked control reactions were performed identically except BMOE was pre-quenched with DTT before cohesin was added to the reaction mixture. Human topoisomerase I DNA supercoiling assays using treated single-chain cohesin were performed as above, with the exception that single-chain cohesin was used at a 10:1 cohesin/plasmid ratio, and NIPBL-MAU2 and STAG1 were added at a 2-fold molar excess over cohesin. Gel images are representative of three independent experiments.

Pre-relaxed plasmid supercoiling assay

For the experiment described in Figures S1F and S1G, in which plasmid DNA was relaxed and purified prior to incubation with cohesin, negatively supercoiled plasmid DNA (pH6HTN) was relaxed by incubating it together with human topoisomerase I for 45 min at 37°C (final reaction conditions: 20 mM Na_2HPO_4/NaH_2PO_4 [pH 7.5], 5 mM Tris [pH 7.5], 25 mM NaCl, 2.5 mM $MgCl_2$, 1 mM DTT, 0.1 mg/mL BSA (Thermo Fisher Scientific; AM2616), 0.4 nM pH6HTN, 3 nM human topoisomerase I in a 600 μL reaction). Reactions were stopped and purified as above and further purified using Ampure XP Reagent (Beckmann; A63881) according to the manufacturer's instructions. This relaxed DNA was then incubated in the presence or absence of human topoisomerase I, cohesin and NIPBL-MAU2 as described in the Human topoisomerase I DNA supercoiling assay section. Gel image is representative of two independent experiments.

Supercoiling handedness experiments

To test whether the plasmids generated in the presence of cohesin-SMC1^{4E} were indeed positively supercoiled, as we assumed, as opposed to representing highly negatively supercoiled plasmids, we performed human topoisomerase I DNA supercoiling assays in the presence of cohesin$^{EQ/EQ}$ or cohesin-SMC1^{4E}, purified this DNA and then incubated it with *E. coli* topoisomerase IV, gyrase or TopA, enzymes that differentially affect negatively and positively supercoiled plasmids (Figure S3A). For these experiments, negatively supercoiled plasmid DNA (pH6HTN) was relaxed by incubating it together with human topoisomerase I for 45 min at 37°C. This mixture was then supplemented with cohesin$^{EQ/EQ}$ or cohesin SMC1^{4E} and NIPBL-MAU2 as indicated and incubated for a further 90 min (final reaction conditions: 20 mM Na_2HPO_4/NaH_2PO_4 [pH 7.5], 5 mM Tris [pH 7.5], 25 mM NaCl, 2.5 mM $MgCl_2$, 1 mM DTT, 0.1 mg/mL BSA (Thermo Fisher Scientific; AM2616), 2 mM ATP (Jena Biosciences; NU-1049), 0.4 nM pH6HTN, 3 nM human topoisomerase I, 6 nM cohesin (corresponding to a cohesin/plasmid molar ratio of 15:1) and 12 nM NIPBL-MAU2 (i.e., a 2-fold molar excess relative to cohesin) in a 600 μL reaction). Reactions were stopped and purified as above and further purified using Ampure XP beads according to the manufacturer's instructions (Beckmann; A63881). 50 ng of this "EQ/EQ DNA" or "SMC1^{4E} DNA" was then incubated with DNA gyrase (Inspiralis; G1001; 0–2 units), *E. coli* Topo IV (Inspiralis; TD002; 0–0.05 units) or *E. coli* TopA (New England Biolabs; M0301L; 0–5 units) for 40 min at 37°C according to manufacturer's instructions. Reactions were stopped, purified and electrophoresed as above. Topo IV relaxed supercoils generated by cohesin-SMC1^{4E} at much lower concentrations than supercoils generated by cohesin$^{EQ/EQ}$ (Figure S3B). Because Topo IV preferentially (though not exclusively) relaxes positively supercoiled DNA,[68–70] these results suggest that plasmids indeed become negatively and positively supercoiled in the presence of cohesin$^{EQ/EQ}$ and cohesin-SMC1^{4E}, respectively. This conclusion is supported by the effects we observed following treatment with DNA gyrase, which does not resolve but instead introduces negative supercoils.[71] When incubated with plasmids supercoiled by cohesin$^{EQ/EQ}$, high concentrations of gyrase converted all slowly migrating DNA bands into one high-mobility species (Figure S3C, lane 6). This effect suggests that plasmids had become negatively supercoiled in the presence of cohesin$^{EQ/EQ}$ and were more negatively supercoiled by gyrase, further increasing their mobility. However, plasmids supercoiled by cohesin-SMC1^{4E} showed a different response to increasing gyrase concentrations (Figure S3C, lanes 7–11). In this case, the fast-migrating plasmids generated in the presence of cohesin-SMC1^{4E} were converted into slower migrating bands at the second highest gyrase concentration but re-converted into a distinct high-mobility species at the highest gyrase dose. This behavior suggests that plasmids had indeed become positively supercoiled in the presence of cohesin-SMC1^{4E} and were gradually converted into negatively supercoiled forms at increasing gyrase concentrations. All gel images are representative of two independent experiments.

The conclusion that plasmids become differently supercoiled in our assays is also supported by the effects that we observed with TopA. This enzyme could only relax plasmids previously incubated with cohesin$^{EQ/EQ}$ (Figure S3D) or negatively supercoiled plasmids isolated from *E. coli* (Figure S3E) but not plasmids previously incubated with cohesin-SMC1^{4E} (Figure S3D). Because TopA can only relax negatively supercoiled DNA,[72] these results indicate that plasmids had become negatively supercoiled in the presence of cohesin$^{EQ/EQ}$, but positively supercoiled in the presence of cohesin-SMC1^{4E}. All gel images are representative of two independent experiments.

For the experiment described in Figure S3E, 50 ng of negatively supercoiled plasmid DNA (pH6HTN (Promega), 4 kb) was incubated with *E. coli* TopA (New England Biolabs; 0–5 units) for 40 min at 37°C according to manufacturer's instructions. Reactions were stopped, purified and electrophoresed as above. All gel images are representative of two independent experiments.

Two-dimensional agarose gel electrophoresis

Supercoiling reactions were set up and purified as described in the Human topoisomerase I DNA supercoiling assay section. Samples were separated in the first dimension on a 0.7% agarose gel in 1x TBE buffer supplemented with 0.1 μg/mL chloroquine for 17 h at 32 V. Gels were incubated with 1 μg/mL chloroquine for 2 h with shaking and were then electrophoresed in the second dimension in 1x TBE buffer supplemented with 1μg/ml chloroquine for 4 h at 64 V. Gels were then stained with Sybr Gold and visualized as above. All gel images are representative of two independent experiments.

High-speed atomic force microscopy

Negatively supercoiled plasmid DNA (pH6HTN) was relaxed by incubating it together with human topoisomerase I for 45 min at 37°C. This mixture was then supplemented with recombinant human cohesin and NIPBL-MAU2 and incubated for a further 90 min (final reaction conditions: 20 mM Na_2HPO_4/NaH_2PO_4 [pH 7.5], 5 mM Tris [pH 7.5], 25 mM NaCl, 2.5 mM $MgCl_2$, 1 mM DTT, 0.1 mg/mL BSA (Thermo Fisher Scientific; AM2616), 2 mM ATP (Jena Biosciences; NU-1049), 1.2 nM pH6HTN, 9 nM human topoisomerase I, 18 nM cohesin (corresponding to a cohesin/plasmid molar ratio of 15:1) and 32 nM NIPBL-MAU2 in a 100 μL reaction). Reactions were stopped and purified as described in the human topoisomerase I DNA supercoiling assay section.

HS-AFM measurements were performed as previously described for dynamic molecules.[73] In brief, a mica sheet was glued to a glass rod (1.5 mm in diameter, 2 mm height, Hilgenberg GmbH) using two-compound epoxy glue (UHU, Bolton Adhesives). The opposite end of the glass rod was attached to the Z scanner using wax. Purified DNA samples were deposited onto a freshly cleaved mica sheet and incubated for 5 min at room temperature. To remove unbound DNA plasmids, the surface was rinsed 5 times with 2 μL imaging buffer (10 mM Tris [pH 8.0], 1 mM EDTA, 12.5 mM $MgCl_2$). DNA plasmids were then visualized in imaging buffer with a scanning HS-AFM (RIBM) operated in tapping mode. The free amplitude was set to 1 nm and the amplitude setpoint to 90% of the free oscillation amplitude. Ultrashort cantilevers (USC-F1.2-k0.15, NanoWorld, Switzerland) with a spring constant of 0.15 N/m, a resonance frequency of around 0.6 MHz and a quality factor of around 2 in liquid were used. All HS-AFM measurements were performed at room temperature.

Magnetic tweezers experiments

Magnetic tweezers experiments were performed using a 3.6 kb torsionally constrained DNA as described.[39] Briefly, for each experiment, 1 pM of the torsionally constrained dsDNA, labeled at one end with biotin and at the other end with digoxigenin, was incubated in PBS buffer for 20 min in an anti-digoxigenin coated flow cell. After washing with 500 μL PBS, 100 μL of streptavidin-coated magnetic beads (Dynabeads MyOne, Invitrogen) were incubated in the flow cell for 5 min. Non-attached magnetic beads were washed out with PBS buffer during flow. Rotation curves in alternating directions were then conducted at 7 pN as previously described[39,50] to identify dsDNA tethers that were singly tethered and torsionally constrained. To determine the degree of DNA twisting generated during loop extrusion on these singly tethered and torsionally constrained dsDNAs, cohesin-SMC1^{4E} and NIPBL-MAU2 were added to the DNA tethers under a constant force of 0.3 pN at room temperature (22°C) (final reaction mixture: 50 mM Tris [pH 7.5], 40 mM NaCl, 2.5 mM $MgCl_2$, 0.25 mg/mL BSA, 1 mM DTT, 0.05% Tween 20, 20 pM cohesin-SMC1^{4E}, 50 pM NIPBL-MAU2, 1 mM ATP). DNA loop-extrusion steps were recorded at 50 Hz via the change in bead Z-position. After 10 min, the timepoint when most DNA loop-extrusion activity had ceased, rotation curves in alternating directions were performed to assess the degree of twist that was introduced at each DNA loop-extrusion step.

Cell extracts and western blotting

For the cell extracts and chromatin fractionation shown in Figures S5A and S5F, cell pellets were resuspended in 20 mM Tris [pH 7.5], 150 mM NaCl, 5 mM $MgCl_2$, 2 mM NaF, 10% glycerol, 0.2% NP-40, 20 mM b-glycerophosphate, 0.5 mM DTT, and cOmplete EDTA-free protease inhibitor cocktail (Merck; 11873580001). Chromatin pellets were separated from whole cell extracts by centrifugation at 2000*g* for 5 min and were washed three times with the above buffer. Genomic DNA in chromatin pellets and in whole cell extracts was digested in the above buffer supplemented with Benzonase (prepared in-house). The cell extracts shown in Figures S5H and S5I were prepared as described[74] in parallel to the vermicelli experiments described in Figures 6A and 6B. The chromatin fractionation shown in Figure S5J was performed as described[42] in parallel to the Hi-C experiments described in Figures 6D–6H and S5K–S5L.

Western blotting was performed using antibodies against SMC1 (generated in-house; A1027), SMC3 (Thermo Fisher Scientific; A300-060A; RRID: AB_67579), WAPL (generated in-house; A1017), Tubulin (Sigma-Aldrich; T5168; RRID: AB_477579), Histone H3 (Cell Signaling Technology; 9715L; RRID: AB_331563), TOP1 (Abcam; ab109374; RRID: AB_10861978), TOP2A (Santa Cruz; sc-166934; RRID: AB_10611755), and TOP2B (Novus Biologicals; NB100-40842; RRID: AB_792364).

Hi-C library preparation

Cells were synchronized in G1 cell cycle stage using two consecutive rounds of treatment with thymidine (2 mM; Sigma-Aldrich) in the presence of 1 μg/mL doxycycline. Two hours prior to release from the second thymidine arrest, cells were treated with auxin

(200 μM; Indole-3-Acetic Acid, Gold Biotechnology) and dTAG7 (1 μM; TOCRIS Bioscience 6912). After washing with pre-warmed medium, cells were incubated with medium containing auxin (200 μM) and dTAG7 (1 μM) for 6 h and harvested for chromatin fractionation and Hi-C ($1x10^7$ cells per Hi-C library). Hi-C library preparation was performed as described.[42]

Vermicelli imaging and pciFRAP

Cells were seeded on chambered cover glass (Nunc 155409) for 2 days in DMEM supplemented with 10% fetal calf serum (Gibco; A5256801), 2 mM L-glutamine (ThermoFisher Scientific; 25030-024), Penicillin-Streptomycin (Sigma-Aldrich; P0781) and 2 μg/mL doxycycline to induce expression of wild type SMC1-FLAG or $SMC1^{4E}$-FLAG. Before imaging SCC1-Halo, cells were incubated with HaloTag TMR ligand (250 μM; Promega) for 20 min. After washing with pre-warmed cell culture medium three times, cells were incubated for 30 min and then exchanged for pre-warmed phenol red free medium supplemented with 10% fetal calf serum (Gibco; A5256801), 2 mM L-glutamine and Penicillin-Streptomycin for imaging. For DNA labeling, cells were incubated with 0.1 μg/mL Hoechst 33342 for 20 min before imaging. Live cell imaging was performed using an LSM880 confocal microscope (Carl Zeiss), equipped with a 40x/1.4 numerical aperture (N/A) oil DIC Plan-Apochromat objective at 37°C and 5% CO_2. For quantification of vermicelli, cells were imaged after the addition of dTAG7 (1 μM final concentration; TOCRIS Bioscience 6912) for 5 h.

pciFRAP was performed essentially as described.[42] Briefly, HaloTag ligand building block (Succinimidyl Ester (O2) Ligand, Promega) was mixed with 1 M Tris-HCl (pH 8.0), incubated for 60 min at room temperature and added to imaging medium (final concentration: 100 μM). Photobleaching half of the nucleus was performed using 2 iterations of a 561 nm diode laser at max intensity after the acquisition of two images. After the bleaching, images were acquired at 1 min intervals for 2 h.

For vermicelli imaging in HeLa cells depleted of TOP1, TOP2AB or WAPL, cells were grown on coverslips in DMEM supplemented with 10% fetal calf serum (Gibco; A5256801), 2 mM L-glutamine (ThermoFisher Scientific; 25030-024) and Penicillin-Streptomycin (Sigma-Aldrich; P0781), treated with dTAG7 (1 μM; TOCRIS Bioscience 6912) and/or auxin (1 μM 5-Ph-IAA; Bio Academia) for 6 h and then fixed for 20 min with 4% paraformaldehyde solution. Cells were permeabilized with 0.1% Triton X-100 in PBS for 5 min and blocked with 3% BSA in PBS supplemented with 0.01% Triton X-100 (PBST) for 30 min. Cells were then incubated with anti-SMC3 antibody (generated in-house; A941) for at least 1 h. After washing with PBST, goat anti-Rabbit IgG Alexa Fluor 488 conjugate (ThermoFisher Scientific; A-11008) was added for 1 h, and nuclei were stained with DAPI for 5 min. The coverslips were then mounted with ProLong Gold Antifade Reagent (ThermoFisher Scientific; P36930) on a microscopy slide and analyzed by microscopy.

QUANTIFICATION AND STATISTICAL ANALYSIS

High-speed atomic force microscopy analysis

Areas of 640 nm × 640 nm were imaged at 500 ms/frame, which typically allowed visualization of one or two DNA plasmids. Each plasmid was imaged for 60 frames and the number of DNA crossings was counted. HS-AFM data was collected using Igor Pro software (Wave Metrics Inc., Lake Oswego, OR, USA). Images were processed by applying mean-flatten and resonance noise correction filters using Kodec software version 4.3.6.16.[75] The statistical details can be found in the figure legends.

Magnetic tweezers analyses

The measured data was analyzed using custom-written Igor v6.37–based scripts.[39,50] All loop-extrusion traces and rotation curves were pooled and filtered to 1 Hz (moving average) for extrusion step identification and Gaussian fitting of the rotations curves. DNA loop-extrusion step sizes were extracted from the change in bead Z-positions in the traces using a previously described methodology and a stepfinder algorithm.[39,50,76] The induced DNA twist during loop extrusion was determined by fitting a Gaussian to the bead Z-positions as a function of applied turns. The peak position of the fitted Gaussian before DNA loop extrusion C_{before} was subtracted from the peak position determined after the DNA loop-extrusion experiments C_{after} which reflect the induced DNA twists $\Delta L_k = \Delta \text{Tw} = C_{\text{after}} - C_{\text{before}}$ in the unit of turns for each trace.

The statistical analyses comparing the degree of DNA twist per LE step were conducted using one-way analysis of variance (ANOVA) with a significance level $\alpha = 0.05$ (95% confidence interval). The statistical details can be found in the figure legends.

1D cohesin supercoiling simulations

We used a fixed-time-step Monte Carlo algorithm for 1D simulations. Each lattice site corresponds to 1 bp and the plasmid was defined with a length of L = 4000 bp, with periodic boundary conditions (lattice site 4000 equals lattice site 0). Simulations were carried out at 297 K (k_BT = 4.1 pN nm). A time step equals one loop-extrusion step, which roughly translates to 0.5 s, based on the ATPase activity of cohesin of roughly 2/protein/s.[10] The simulation was run for 1800 time steps (~15 min) using the DelftBlue supercomputer.[77]

For every time step, the following modules are executed.

Cohesin complexes spawn
Cohesin lifetime and direction lifetime assignment

Cohesin stepping
Linking number fixation by topoisomerase
Cohesin dissociation

Cohesin complexes spawn

Cohesin complexes have a uniform binding probability in the absence of any accumulated twist (i.e., for the first cohesin complex binding to the plasmid). If twist has been accumulated in the plasmid, the cohesin complex binds to a positively supercoiled segment with a 79% probability.[24] The binding rate of cohesin to the plasmid, k_{on}, was varied over several orders of magnitude between 1×10^{-5} and $1\ x10^2$ and the number of cohesin complexes on the plasmid was counted during the simulation, which was used to evaluate the cohesin/plasmid ratio in simulations and to compare to experiments (e.g., Figure S4B).

Cohesin lifetime and direction lifetime

Upon binding, the lifetime of the cohesin complex is drawn from an exponential distribution with mean $1/k_{off}$. Furthermore, cohesin complexes move directionally and can switch directions with rate constant $k_{switch} = 0.025\ s^{-1}$ (roughly once or twice per minute) and direction lifetimes are drawn from an exponential distribution with mean $1/k_{switch}$.

Cohesin stepping

All plasmid-bound cohesin complexes attempt to make a step in random order during one time step of the simulation. Each cohesin takes a step of $\Delta l = 150$ bp,[57] enlarging its loop, while a twist of $\Delta Tw = -0.6$ is added to the loop. If the segment on which the step is being made has a non-zero twist itself, a part of this twist is transferred into the loop. The relative twist per bp in a segment s is $rTw_s = Tw_s/L_s$, where Tw_s is the accumulated twist and L_s is the length of segment s. The twist transferred into the loop while the loop s is being enlarged on the expense of segment s is $\Delta Tw = -0.6+\Delta L\cdot rTw_s$. Concomitantly, a twist of $\Delta Tw = +0.6-\Delta L\cdot rTw_s$ is added to segment s (illustrated in Figure S4A). Note that region s may also be a previously extruded loop such that the loading of the next SMC produces nested loops. Cohesin complexes are allowed to traverse one another[78] and generate Z-loops while doing so. If Z-loops are generated, twist is added to the resulting Z loop delimited by the two loop anchors defining the Z-loop. Similarly, Z loops can be resolved by nesting loops. The loop anchors are modeled as twist diffusion barriers.

After every potential move, the resulting torque τ in the loop as well as in segment s is computed via[79] $\tau = 2\pi k_B TC\cdot Tw/L_c$, where $C = 100$ nm is the twist persistence length of dsDNA,[80] and $L_c = L\cdot 0.342$ nm/bp denotes the contour length of the plasmid. If the torque in all concerning segments remains below the stall torque, τ_{stall}, the move is accepted and rejected otherwise. Even though not measured, cohesin complexes must have a stall torque which is lower than the energy of ATP binding to the complex. Here we set $\tau_{stall} = 12\ k_BT$, slightly above the energetic cost to extrude DNA.[19,81]

Linking number fixation

Topoisomerases bind to the plasmid at a rate k_{topo}. The binding position is drawn from a uniform distribution across the plasmid. Human topoisomerase I is able to relax both positive as well as negative supercoils up to a maximum of $\Delta L_k = 27$,[82] or all linking numbers if the segment topoisomerase bound to contains fewer linking numbers.

Cohesin dissociation

When a cohesin complex lifetime reaches zero, it dissociates from the plasmid. If a Z-loop is associated with the segment, this Z-loop is first resolved upon which the loop dissolves. The loop length and its twist merges with its surround segment whose relative twist and torque is updated.

Sensitivity to parameter choices

We varied the dissociation and the topoisomerase action rate, k_{off} and k_{topo}, respectively. The results are qualitatively similar as long as the topoisomerase activity is not too low (e.g., $k_{topo} = 10^{-3}$/step causes only 1–2 topoisomerase actions per simulation run yielding only low amounts of fixed linking numbers (Figures S4I and S4J).

Plectoneme formation

Twist can be converted into writhe via the formation of plectonemes and small chiral loops (“curls”), which might not be readily relaxed by human topoisomerase I.[83] To assess the potential impact of plectoneme formation on the resulting ΔL_k of the plasmids after cohesin-mediated twisting and ΔL_k fixation by human topo I, we computed the distribution of ΔL_k into twist Tw and writhe Wr according to $\Delta L_k = \Delta Tw + \Delta Wr$ in every cohesin-delimited segment of length L in every step of the simulation before topoisomerases act on the plasmid. To do this, we followed a mesoscopic model,[84] which describes the buckling transition and the number and size of plectonemic domains that are likely to form, given a linking number ΔL_k in a segment of length L. The DNA segment of length L is partitioned into twisted DNA of length L_s, plectonemic DNA of length L_p, m plectoneme “tails” Γ, and n curls of length γ: $L = L_s + L_p + m\Gamma + n\gamma$ (see Figure 1 in[84]). Here, m denotes the number of plectonemes and n denotes the number of curls. The free energy, F, is the sum of the energetic contributions of the twisted DNA F_s, the plectonemic DNA F_p, the curls F_c, and an entropic term that accounts for the fact that plectonemes and curls are randomly positioned along the segment length: $F(n,m,L_p) = F_S + F_p + F_c - TS_m$. Note that all energetic contributions depend on the number of plectonemes (m) and curls (n), as well as on the length of DNA absorbed into plectonemes. The contribution of twisted DNA is only counted over the segment length that is not in the plectonemic and curl regions. We refer the reader to eq. (12) in Marko and Neukirch[84] for the expression of $F(n,m,L_p)$, but note that all contributions to F also depend on the externally applied force f. The implementation was validated using forces presented in Marko and Neukirch[84] and subsequently extrapolated to f = 0.05 pN for our simulations since the model diverges for $f \rightarrow 0$ pN.

The plectonemic contribution to the energy, F_p, depends on the plectoneme geometry via its parametrization using the plectoneme radius r and pitch angle α. The values of the plectoneme radius and pitch angle were determined via energy minimization of $F_p(\Delta L_{kp}, m, L_p, f, r, \alpha)$ for a given set of constraints ΔL_{kp}, m, L_p, and f, where ΔL_{kp} is the linking number in the plectonemic region. Minimization of F_p was implemented using *scipy.optimize.minimize*.[85] The optimization of F_p to obtain r and α was too computationally expensive to calculate "on-the-fly" during the simulations at every time step. Instead, we evaluated F_p in a separate optimization routine for values of ΔL_{kp}, m, and L_p that could be encountered in the simulations (the force f was set to either 2 pN, 1 pN, 0.5 pN, or 0.25 pN to validate our implementation using the data described in[84] or to 0.05 pN for our simulations). We varied ΔL_{kp}, m, and L_p over a grid spanning $|\Delta L_{kp}|_{grid} = [0, 0.1, \ldots, 20]$, $m_{grid} = [1, 2, \ldots, 10]$, and $L_{p,grid} = [0\text{ nm}, 0.5\text{ nm}, \ldots, 200\text{ nm}]$ and minimized F_p to generate a lookup table for the optimal values of r and α over the (discrete) parameters $\Delta L_{kp,grid}$, m_{grid}, and $L_{p,grid}$. In order to evaluate the plectonemic energetic distribution during the Monte Carlo simulations given a set of ΔL_{kp}, m, and L_p, the optimized r and α values for which $|\Delta L_{kp,grid} - \Delta L_{kp}| + |m_{grid} - m| + |L_{p,grid} - L_p|$ is minimum are used.

Having the free energy of any state defined by $F(n,m,L_p)$ (note that ΔL_k, L, f, r, and α are implicit parameters of $F(n,m,L_p)$), the partition function $Z = \sum_X e^{-\beta F(X)}$ ($1/\beta = k_B T$) was computed by summing over all states $X=(\Delta Lk, L, f)$:

$$Z(\Delta L_k, L, f) = \sum_{n=0}^{L/\gamma} e^{-\beta F(n,0,0)} + \sum_{m=1}\sum_{n=0}\sum_{L_p/d=1}^{[L-n\gamma-m\Gamma]/d} \frac{d}{D} e^{-\beta F\left(n,m,L_p\right)}$$

The first term considers straight DNA with curl fluctuations along it and the second term considers variable numbers of plectonemic domains ($m > 0$), where the sum over L_p is carried out with a mesh size d = 1 nm. The factor of D accounts for the indistinguishability of plectoneme states that differ by less than D in length. Finally, all the sums are subject to the constraint that the regions involved in curls and plectonemes should not exceed the total length L: $n\gamma + m\Gamma + L_p \leq L$.

Using the partition function Z, we can compute the average values $\langle m \rangle, \langle n \rangle$, and $\langle L_p / m \rangle$ (the latter denotes the average amount of plectonemic DNA per plectonemic region), according to eq. (14c-14e) in[84], given ΔL_k and L (and a constant force f = 0.05 pN as mentioned above). The part of the linking number ΔL_k in the segment of length L equals the sum of the writhe absorbed into n curls ($Wr_c = nw_c \approx n$; see eq. (A.1) in[84]) and the writhe absorbed into m plectonemic regions (each contributes a writhe $Wr_p = L_p \sin(2\alpha)/(4\pi r) + mw_p$, see eq. (5) and (A.4) in[84]). The remaining fraction of ΔL_k that is not transferred into writhe remains present as twist. Note that $\langle m \rangle$ and $\langle n \rangle$ are not necessarily integers. To stochastically determine integer values of m and n at a particular step and segment of a simulation, we determined m (and n analogously) via the formula $m = \lfloor . \langle m \rangle \rfloor + (R < (\lfloor . \langle m \rangle \rfloor - \langle m \rangle))*1$ where $\lfloor . \langle m \rangle \rfloor$ denotes the largest integer value of $\langle m \rangle$ and R is a uniform random number on the interval (0,1). For instance, for $\langle m \rangle = 1.3$ and R = 0.1, the term $(R < (\lfloor . \langle m \rangle \rfloor - \langle m \rangle))*1 = (0.1 < (1\text{–}1.3))*1 = (0.1 < 0.3)*1 = (\text{True})*1 = 0$ and thus m = 2. If the drawn random number R = 0.5, then $(R < (\lfloor . \langle m \rangle \rfloor - \langle m \rangle))*1 = (0.5 < 0.3)*1 = (\text{False})*1 = 0$ and thus m = 1. In other words, m (and n) will be rounded up from $\langle m \rangle$ (and $\langle n \rangle$, respectively) with a probability equal to its decimals.

We performed simulations as described above and included an additional module which computes the distribution of ΔL_k into twist and writhe. Since we considered that type I topoisomerases cannot relax writhe, transfer of ΔLk into writhe can only reduce the amount of twist that topoisomerases encounter in the simulations. For simulations using $k_{off} = 10^{-3}$/step and $k_{topo} = 10^{-1}$/step, we found that the inclusion of a transfer of ΔL_k into writhe does not affect the outcome of the supercoiling simulations (Figure S4G). The reason for this is that the majority of the simulations did not evoke any writhe in 232/360 (64.4%) (Figure S4H; here we varied k_{on} from 10^{-5} to 10^2/step and repeated the simulations for each combination of parameters 20 times). For the ~35% of the simulations in which $Wr > 0$, typically less than 1% of the simulated SMC translocations were affected by the generation of writhe, even though occasionally up to 10% of the SMC translocations were affected (Figure S4H). The writhe absorbed in these simulations was frequently found to be at the lower limit for plectoneme/curl generation ($|Wr| \approx 1$) but rose to up to $|Wr| \sim 6$. We noted that the generation of writhe mostly affected simulations in which few SMCs were included (i.e., at low k_{on}), likely because segments along the plasmid become small when many SMCs act on the plasmid and do not allow the formation of curls/plectonemic regions.

We conclude that the generation of writhe has a negligible effect in our simulations. All results presented in Figure S4 (with the exception of Figures S4G and S4H) were therefore computed under the assumption that all excess linking number ΔL_k is stored in the individual segments exclusively as twist (and not as writhe).

Hi-C data processing

Illumina sequencing was performed on all Hi-C libraries with 150 bp paired-end reads. Two replicate datasets for each library were truncated, filtered, and aligned against the human genome assembly hg19 (GRCh37) using bowtie2 and the HiCUP processing pipeline version 0.7.4,[86] and then merged. Alignments were converted into input for juicer_tools pre (juicer_tools version 1.22.01[87] as well as input for HOMER version 4.11[88]). All juicer-based contact matrices used for analysis were Knight-Ruiz normalized. Loop annotation and merging was performed using "juicer_tools hiccups" at the default resolution. TAD annotation and insulation scores were generated using the "findTADsAndLoops.pl" script in HOMER, which scans the relative contact matrices for locally dense regions of contacts or areas with an increased degree of intra-domain interactions. Plots of insulation profiles were made using insulation scores in the bedGraph file format and TAD boundary coordinates from regions around these coordinates. Aggregate peak analysis of Hi-C peaks called by hiccups was performed using "juicer_tools apa." The Hi-C looping peaks detected in all conditions were classified according to their size and used as coordinates for aggregation within Hi-C maps. These aggregated size-classified

Hi-C peaks were visualized by plotting the cumulative stack of sub-matrices such that the Hi-C peaks lie at the center of the matrix. The resulting APA plot displayed the abundance of contacts respective to local contact density.

Vermicelli quantification

Vermicelli in SMC1 WT and SMC1 4E-expressing HeLa cells were quantified by calculating coefficient of variation using a custom Python script as described.[42] Briefly, the central image within each z stack was determined by identifying the image with the highest mean pixel intensity in the DNA channel. A binary mask of this image was then created and applied to the images at this Z position in the Scc1 and DNA channels. The mean and standard deviation of the pixel values within this mask were then calculated in both channels. The coefficient of variation for the Scc1 channel was then calculated by dividing the standard deviation by the mean. The statistical details can be found in the figure legends.

Vermicelli in HeLa cells depleted of TOP1, TOP2AB were enhanced by applying the "Tubeness" filter[89] to the SMC3 channel in ImageJ (NIH) and converted to a binary mask. This mask was used to create a distance map between vermicelli; the mean value of this inter-vermicelli distance per cell reflected the degree of vermicelli formation and was plotted in Figure 5C. The statistical details can be found in the figure legends.

pciFRAP analysis and curve fitting

The fluorescent recovery kinetics were quantified using the ZEN2011 software, as the difference between the mean fluorescence signal intensity of the bleached and the unbleached regions followed by background subtraction. pciFRAP curves were normalized to the mean of the pre-bleach fluorescent intensity and to the first image after photobleaching. G1 and G2 phase cells were identified by nuclear or cytoplasmic localization of DHB-mVenus signals, respectively.[90] iFRAP curves were fitted using the single exponential function f(t) = EXP(-kOff1*t) or the double exponential function f(t) = a*EXP(-kOff1*t)+(1-a)*EXP(-kOff2*t) in R using the mini-pack.lm package (version 1.2.1). Double exponential curve fitting was performed under the constraints that 1/kOFF1 (the dynamic residence time) and 1/kOFF2 (the stable residence time) were in the range of 1–40 min and 5–15 h, respectively. The statistical details can be found in the figure legends.